Physics Department
Faculty of Natural Sciences
Ben-Gurion University of the Negev

The Physics of Nitrogen-Vacancy Color Centers in Diamonds and their Interaction with External Fields

Thesis submitted in partial fulfilment of the requirement for the degree of Master of Science in the Faculty of Natural Sciences

Submitted by: **Yossi Rosenzweig**
Advisor: **Prof. Ron Folman**

March 2016

Physics Department
Faculty of Natural Sciences
Ben-Gurion University of the Negev

The Physics of Nitrogen-Vacancy Color Centers in Diamonds and their Interaction with External Fields

Thesis submitted in partial fulfillment of the requirement for the degree of Master of Science in the Faculty of Natural Sciences

Submitted by: **Yossi Rosenzweig**
Advisor: **Prof. Ron Folman**

Signature of student: _____Date:_____
Signature of supervisor:_____Date: _____
Signature of chairperson of the committee for graduate studies:
_____Date: _____

March 2016

Abstract

The optically-detected magnetic resonance spectroscopic technique (ODMR) is currently the main tool for investigating nitrogen vacancy (NV) centers in diamond.

In this thesis we introduce a novel spectroscopic technique, analogous to Doppler-free spectroscopy used in atomic vapor cells. While there is no "velocity distribution" in the solid diamond lattice, there is a distribution of transition frequencies due to the local environments to which each individual NV center is exposed. The broadened transition line could come, for example, from local strain or from local magnetic fields, and just as in the case of atomic vapor, it too causes inhomogeneous broadening to be observed in the spectroscopy of the sample. Understanding the exact origin of the local environment is of great importance both for future fundamental studies with this system and for technological applications. Here, we use the above novel technique to provide additional insight concerning the actual origin of the inhomogeneous broadening.

Furthermore, we demonstrate, in good agreement with theory, narrower linewidths with this technique as compared to standard ODMR linewidths. This may be useful in future technological applications such as magnetometry.

Abstract in Hebrew

Acknowledgments

First and foremost i would like to thank my adviser Prof. Ron Folman for taking me through the rabbit hole into the wonderful world of quantum optics and experimental physics. Your creativity, passion and precision are a lesson for life. Thank you Ron for giving me such a great opportunity.

I would also like to thank my close colleague, Ph.D student Yechezkel Schlussel for teaching me all the small secrets of experimental work while helping me with my experiments, as well as encouraging me with his funny stories. Your good mood always brightened up even the toughest day. I would also like to thank the rest of the NV team: Dr. Armin Biess for not taking things as granted, Dr. Judith Kupferman for correcting my English mistakes (among others) and undergrad student Daniel Beer for sharing with me his knowledge in electrical engineering.

I would not complete this thesis without the help of Dr. Menachem Givon who guided me through the administration of this thesis. In addition I would like to thank Dr. David Groswasser for his time in the past year and his good experimental insights. A very special thanks is to Eng. Zina Binshtok for the instruments that she built for me, her willings to answer even the simplest question in electronics and just as important- her good math riddles. I would also like to thank the rest of our atom-chip group at BGU.

I would also like to thank my parents for their endless support and love. They always believed in me, even when I did not. Thank you. I love you. Thanks you Yehudit, Yair, and Hanan, my brothers and sister for your great humor and for putting my complaints in perspective. You guys are the best.

Finally, last in acknowledgments but first in heart and mind, I would like to thank my wife Nechama for encouraging me when I was about to fall, drive me when I was too much at ease, and love me no matter what. Thank you. Thank you Yotam and Noam, my two beautiful boys. You are the sunshine of my life. There was not a single day in which I had to work until late hours, after which I did not pass by your beds when i got home, kissed you quietly, made sure that you are covered and prayed that you will always be happy.

Contents

List of Figures

List of Tables

Abbreviations

FWHM full-width at half-maximum
AOM acousto-optic modulator
NV negatively charged nitrogen vacancy
HF hyper-fine
ISC intersystem crossing
MO molecular orbitals
IR irreducible representation
HPHT high-pressure high-temperature
CVD chemical vapor deposition
MW microwave
PBS polarizing beam splitter
HWP half-wave plate
QWP quarter-wave plate

Introduction

The NV is an "atom-like" solid state system; although the system is highly localized inside a diamond lattice, it exhibits atom-like properties such as narrow energy levels with a sharp spectroscopic line, spin, the possibility of optical pumping, long coherence times, etc. The combination of these properties yields a unique sensor, with both high spatial resolution and sensitivity [2].

The spectroscopic linewidth of the NV microwave (MW) transition in the ground state plays an important role when probing magnetic fields, as the sensitivity of the NV is proportional to $\sqrt{\frac{\Gamma}{N}}$, where Γ is the spectroscopic full-width at half-maximum (FWHM) line and N is the number of NVs being probed. In ODMR spectroscopy of NVs there are many reasons for a broadened line shape, starting from the natural linewidth, through MW power broadening and ending with inhomogeneous broadening. Understanding the origins of the latter is interesting scientifically, and may be useful for both fundamental and technological studies; and is the topic of this thesis.

In this thesis we show that inhomogeneous broadening originates from a variance of the local magnetic environment felt by each NV in the probed ensemble. To this end, we have developed a novel spectroscopic technique based on "Doppler-free" spectroscopy done in vapor: we scan around a specific hyperfine (HF) transition between two Zeeman sub-levels with two MW fields, pump and probe, that have a fixed frequency gap between them, $\Delta f = f_{m_s=+1;m_I=0} - f_{m_s=-1;m_I=0}$, where m_s is the spin projection of the Zeeman eigenstate, m_I is the projection of the nitrogen nuclear spin and defines the HF states, and f represents the transition frequency. The consequence of the fixed frequency gap which we impose is that each of the two radiation fields interacts with a different population (i.e., different local magnetic field) when we scan around the $|m_s = -1; m_I = 0\rangle$ transition giving rise to a regular ODMR line shape. However, as we approach resonance, both pump and probe fields address the same population, yielding a narrow "Doppler-free" type hole inside the broadened MW transition line and proving that the main contribution to the broadening originates from the local magnetic environment in the diamond lattice.

In Chapter 1 we present the theoretical background required to understand the NV system, including the geometrical structure of the NV inside the diamond, and describe its energy levels using both a group-theory approach and the Hamiltonian. In Chapter 2 we introduce our experimental setup. We use our setup in Chapter 3 to demonstrate and explain the ODMR technique, and its relation to magnetic sensitivity. With this technique we calibrate the system for best parameters. In Chapter 4 we show, using saturation spectroscopy, that the main cause of inhomogeneous broadening is the local magnetic field. Unfortunately, the results obtained with the latter technique suffer from instabilities and are therefore not fully persuasive, and consequently we have devised an alternative path that utilizes a new spectroscopic technique in NV centers that clearly identifies the local magnetic fields as the source for the observed inhomogeneous broadening. The results are presented in Chapter 5 in good agreement to theory. We also show that the new method provides a narrower linewidth. We summarize and conclude in Chapter 6. In the three appendices, we describe the technical details of the AOM setup, explain the observation of side-dips, and present an outlook with ideas for future experiments.

Chapter 1

Theoretical Background

In order to understand the physics of the NV system, we start by describing the system's geometrical structure and symmetry and apply the group theory approach to associate the different energy levels with different symmetries. The different symmetries will give us selection rules and in particular they will show that the transition between state $^3A_2$ (ground state) to ^3E (excited state) is dipole allowed and can be accessed via green light. We then describe the Hamiltonian of the $^3A_2$ level, and show that since the decay process from ^3E has a preferable sublevel in $^3A_2$, we can polarize the system into a specific quantum state simply by applying green laser light.

1.1 NV Structure and its Symmetry

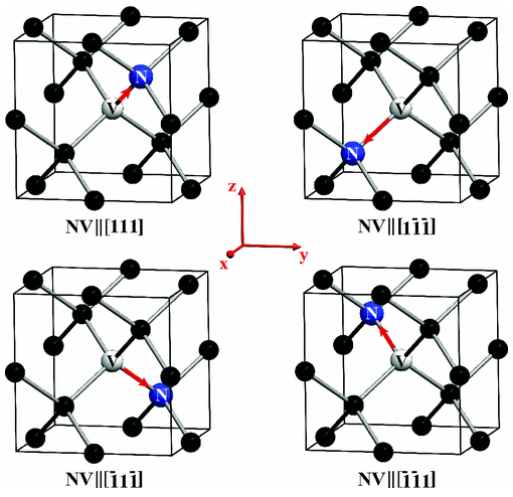

(a) The four possible orientations of the NV center. Carbon atoms are labelled in black, nitrogen atoms in blue, and vacancies in white. The NV axis is indicated by red arrows. Taken from [3].

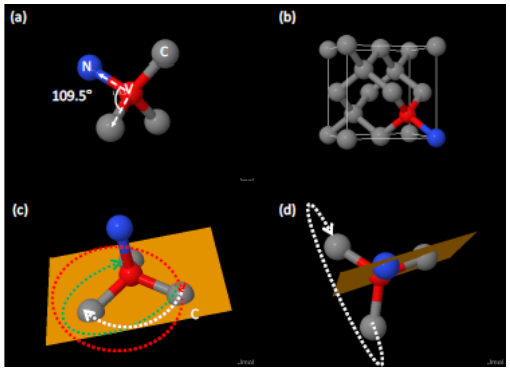

(b) NV system symmetry. Nitrogen in blue, vacancy in red, and carbons are in grey. (a) The general geometrical structure of the NV system. (b) The system inside a diamond unit cell. (c) The three rotational symmetries. (d) One of the three reflection symmetry operations. Another two planes of reflection are not presented. Taken from [1].

Figure 1.1

An NV center is formed inside a diamond lattice when a substitutional nitrogen atom has an adjacent vacancy as its nearest neighbor. This structure can appear in natural diamond, but in very low concentrations [4], making the high-pressure high-temperature (HPHT) and chemical vapor deposition (CVD) synthetic diamonds more popular candidates for NV experiments. Typical NV density can be 1 ppm in HPHT synthetic diamond (1 ppm $\simeq 1 \times 10^{17}\,\mathrm{cm}^{-3}$ in diamonds) and roughly 0.04 ppm in CVD [5]. The NV density can be improved dramatically (e.g. 100 ppm in

HPHT diamond) by increasing the nitrogen and vacancy densities, and mobilizing the vacancies until they are trapped near a nitrogen impurity. The amount of nitrogen in the sample can be controlled during the synthetic process or during the creation of vacancies (natural diamonds too have nitrogen impurities, which are the most common impurity found in diamonds). In order to create vacancies we use special treatment such as irradiation damage, where high-energy particles penetrate the diamond and increase the amount of vacancies. Finally we use annealing to transport the vacancies until they are trapped near nitrogen impurities [6] consequently increasing the NV density in the diamond. The annealing temperature is usually around 800°. For the irradiation process we use high energy particles such as electrons and ions, typically in the MeV regime, although in near-surface experiments where NVs must be placed just a few nm away from surface, we use particles with lower energies of several keV [7]. By controlling the energy of the particle beam, one can create NVs at different depths [8] which may come handy in certain experiments, as can be seen in [9].

The entire NV complex is constructed from the nitrogen-vacancy couple as well as the 3 nearest neighbours of the vacant site. This structure has a specific symmetry: we can rotate the system around the N-V axis at 120°, 240°, 360° and leave the system unchanged. There is also a reflection symmetry operation around the three possible planes that contain the nitrogen atom, the vacancy and one of the carbon atoms, thus yielding a point defect with a C_{3v} symmetry (Fig. 1.1b). In addition, we can exchange each of the 3 carbon atoms with the nitrogen atom and still retain the same structure, except that now the principal symmetry axis (the NV axis) will have a different orientation with a 109° angle. This gives a total of 4 possible orientations of the NV inside the diamond lattice (Fig. 1.1a).

In terms of chemical bonding, each carbon atom in a diamond lattice has 4 electrons in its outer shell, leading to covalent bonding with each of its 4 carbon neighbors, giving a total of 8 electrons in the valance shell and thus making it a full shell. When we replace 2 carbon atoms with a nitrogen atom and adjacent vacant site, the vacant site has 4 "dangling bonds" with its neighbors which have a total of 5 available electrons: 3 electrons come from the 3 carbon neighbors and the remaining 2 come from the nitrogen atom as it has one more electron than the carbon atom in its outer shell. Since a 6-electron system is preferable, a 6th electron is trapped, presumably from another nitrogen impurity donor [10], making an even-electron-number system [11] that is often treated as a two-hole system.

NV centers that have 5 electrons are known as NV^0 and will be ignored in this thesis. The 6-electron structure is a negatively charged nitrogen vacancy center denoted as NV^-. Throughout this thesis, since we study only the negatively charged structure, we will refer to it just as NV.

1.2 Group Theory Approach

The fact that the system has a certain symmetry gives us information about the symmetries of the different wave functions and the selection rules that govern the transitions between them. In solid state physics, we usually describe the electron wave function in the lattice using the Bloch wave function: $\Psi(\mathbf{r}) = e^{i\mathbf{k}\cdot\mathbf{r}}u(\mathbf{r})$, where $\mathbf{r}$ is position, $\mathbf{k}$ is the crystal vector, and $u(\mathbf{r})$ is some periodic function [12]. But in the presence of a defect, translation symmetry is broken and the symmetry is reduced (to a point group symmetry in our system). In such symmetry, the Bloch wave function solution is not valid anymore and we need to come up with a new wave function basis.

In order to find the behavior of the NV wave function, we shall use the powerful tool of group theory. According to group theory, the wave functions of a system can be characterized by the way that they transform under the symmetry operations of the system and this yields selection rules. We assume that there is a set of symmetry operations which are also unitary transformations $\{\hat{U}_k\}$, and that the Hamiltonian is invariant under all those transformations and all the symmetry

operations of the Hamiltonian are included in that group. We then find that

$$\hat{U}_k \hat{\mathcal{H}} \hat{U}_k^\dagger = \hat{\mathcal{H}}\,, \tag{1.1}$$

for every $\hat{U}_k$. This group of operations consists of the elements presented in Fig. 1.1 (i.e., $\{E,R_1,R_2,R_3,C_3,C_3^{-1}\}$ where E is the identity operation, C_3 is rotation operation and R_i is the reflection operation). We can rewrite the Schrödinger equation

$$\hat{\mathcal{H}}|\Psi_n\rangle = E_n|\Psi_n\rangle\,,$$

as

$$\hat{U}_k \hat{\mathcal{H}} \hat{U}_k^\dagger|\Psi_n\rangle = E_n|\Psi_n\rangle\,,$$

and if we apply one of the symmetry operations, i.e., multiply by $U_k^\dagger$ from the left, we obtain:

$$\mathcal{H} U_k^\dagger|\Psi_n\rangle = E_n U_k^\dagger|\Psi_n\rangle\,. \tag{1.2}$$

The existence of a symmetry group for the system raises the possibility of degeneracy. We can see that the new eigenstates, $U_k^\dagger|\Psi_n\rangle$, must have the same energy after applying the C_{3v} symmetry operations on $|\Psi_n\rangle$. Unless $U_k^\dagger|\Psi_n\rangle = C|\Psi_n\rangle$ for all $U_k^\dagger$, the level is degenerate [13]. The new eigenfunctions $U_k^\dagger|\Psi_n\rangle$, or just $|\Psi_n^k\rangle$, could have duplicates. The distinct degenerate eigenstates are related by $|\Psi_n^k\rangle = \sum_l M_{k,l}|\Psi_n^l\rangle$ where the M matrices are the irreducible representations (IR) of the symmetry group. We can match to each eigenfunction of the Hamiltonian a set of IR M matrices, thus classifying each eigenfunction by its IR.

In order to find the irreducible representation (IR), we begin by looking at our system and trying to understand the reducible representation. When we have a vacancy in a lattice, the absence of an atom breaks the bonds of the neighboring atoms to create so called "dangling bonds" to the vacancy. The orbitals of each atom get hybridized to sp^3 orbitals. We label the orbital that points to the vacant site as σ_i, where $i = 1, ..., 4$, and we associate σ_1 with the orbital of the nitrogen atom and σ_i $(i = 2, ..., 4)$ with the three carbon neighbours. (Notice that we take only one orbital from each atom. The other sp^3 orbitals of each atom interact with carbons outside the NV structure, and we ignore them.) We can represent each orbital using a vector, where $\sigma_1 = \begin{pmatrix}1\\0\\0\\0\end{pmatrix}$, $\sigma_2 = \begin{pmatrix}0\\1\\0\\0\end{pmatrix}$, $\sigma_3 = \begin{pmatrix}0\\0\\1\\0\end{pmatrix}$ and $\sigma_4 = \begin{pmatrix}0\\0\\0\\1\end{pmatrix}$, but in this basis, the representation of the symmetry operations is not block-diagonal, as can be seen in Table 1.1. In order to extract the IR from the reducible representation, we can use the following transformation matrix:

$$R = \begin{pmatrix} 1 & 0 & 0 & 0 \\ 0 & -\sqrt{\frac{2}{3}} & \sqrt{\frac{1}{6}} & \sqrt{\frac{1}{6}} \\ 0 & 0 & -\sqrt{\frac{1}{2}} & \sqrt{\frac{1}{2}} \\ 0 & -\sqrt{\frac{1}{3}} & -\sqrt{\frac{1}{3}} & -\sqrt{\frac{1}{3}} \end{pmatrix}.$$

We perform an homomorphism transformation on the symmetry operation representation in Table 1.1 and simultaneously form block diagonal matrices (i.e. IR) from all the symmetry operation representations [14]. The result of the transformation $R\Gamma R^{-1}$, where Γ is a reducible symmetry operation as listed in Table 1.1, is presented in Table 1.2.

$\Gamma(E)$	$\Gamma(C^+)$	$\Gamma(C^-)$	$\Gamma(\sigma_v)$	$\Gamma(\sigma_v')$	$\Gamma(\sigma_v'')$
$\left(\begin{array}{c\|ccc} 1 & 0 & 0 & 0 \\ \hline 0 & 1 & 0 & 0 \\ 0 & 0 & 1 & 0 \\ 0 & 0 & 0 & 1 \end{array}\right)$	$\left(\begin{array}{c\|ccc} 1 & 0 & 0 & 0 \\ \hline 0 & 0 & 0 & 1 \\ 0 & 1 & 0 & 0 \\ 0 & 0 & 1 & 0 \end{array}\right)$	$\left(\begin{array}{c\|ccc} 1 & 0 & 0 & 0 \\ \hline 0 & 0 & 1 & 0 \\ 0 & 0 & 0 & 1 \\ 0 & 1 & 0 & 0 \end{array}\right)$	$\left(\begin{array}{c\|ccc} 1 & 0 & 0 & 0 \\ \hline 0 & 1 & 0 & 0 \\ 0 & 0 & 0 & 1 \\ 0 & 0 & 1 & 0 \end{array}\right)$	$\left(\begin{array}{c\|ccc} 1 & 0 & 0 & 0 \\ \hline 0 & 0 & 0 & 1 \\ 0 & 0 & 1 & 0 \\ 0 & 1 & 0 & 0 \end{array}\right)$	$\left(\begin{array}{c\|ccc} 1 & 0 & 0 & 0 \\ \hline 0 & 0 & 1 & 0 \\ 0 & 1 & 0 & 0 \\ 0 & 0 & 0 & 1 \end{array}\right)$

Table 1.1: Representations of the C_{3v} point group symmetry operations. $\Gamma(C^+)/\Gamma(C^-)$ represents rotation of $120°/-120°$ around the nitrogen atom, σ sign represents reflection around a plane that contains the nitrogen atom and one of the carbon atoms and $\Gamma(E)$ represents the identity operation. We mark the fact that the nitrogen is not affected by any operation, by using the 1×1 block diagonal matrices. It is clear that the 3×3 matrices that operate on the carbons are not the smallest block diagonal matrices that we can generate for any operation except for the trivial identity operation $\Gamma(E)$.

$\Gamma(E)$	$\Gamma(C^+)$	$\Gamma(C^-)$	$\Gamma(\sigma_v)$	$\Gamma(\sigma_v')$	$\Gamma(\sigma_v'')$
$\left(\begin{array}{c\|ccc} 1 & 0 & 0 & 0 \\ \hline 0 & 1 & 0 & 0 \\ 0 & 0 & 1 & 0 \\ 0 & 0 & 0 & 1 \end{array}\right)$	$\left(\begin{array}{c\|ccc} 1 & 0 & 0 & 0 \\ \hline 0 & -\frac{1}{2} & -\frac{\sqrt{3}}{2} & 0 \\ 0 & \frac{\sqrt{3}}{2} & -\frac{1}{2} & 0 \\ 0 & 0 & 0 & 1 \end{array}\right)$	$\left(\begin{array}{c\|ccc} 1 & 0 & 0 & 0 \\ \hline 0 & -\frac{1}{2} & \frac{\sqrt{3}}{2} & 0 \\ 0 & -\frac{\sqrt{3}}{2} & -\frac{1}{2} & 0 \\ 0 & 0 & 0 & 1 \end{array}\right)$	$\left(\begin{array}{c\|ccc} 1 & 0 & 0 & 0 \\ \hline 0 & 1 & 0 & 0 \\ 0 & 0 & -1 & 0 \\ 0 & 0 & 0 & 1 \end{array}\right)$	$\left(\begin{array}{c\|ccc} 1 & 0 & 0 & 0 \\ \hline 0 & -\frac{1}{2} & -\frac{\sqrt{3}}{2} & 0 \\ 0 & -\frac{\sqrt{3}}{2} & \frac{1}{2} & 0 \\ 0 & 0 & 0 & 1 \end{array}\right)$	$\left(\begin{array}{c\|ccc} 1 & 0 & 0 & 0 \\ \hline 0 & -\frac{1}{2} & \frac{\sqrt{3}}{2} & 0 \\ 0 & \frac{\sqrt{3}}{2} & \frac{1}{2} & 0 \\ 0 & 0 & 0 & 1 \end{array}\right)$

Table 1.2: IR of the C_{3v} point group. The 1×1 blocks are said to have A_1 symmetry if they are completely symmetric and A_2 if they are antisymmetric with respect to reflection. The 2×2 blocks are said to have E symmetry (not to be confused with the identity symmetry operator $\Gamma(E)$) and represent two degenerate eigenfunctions.

Now that we have the IR, we can find the eigenfunction that transforms as one. This can be done using the projection operator [15]:

$$\phi_r = \frac{l_r}{h}\sum_e \chi_e^r R_e \sigma_i \,, \tag{1.3}$$

where l_r is the order of the IR r, h is the number of group elements, χ_e^r is the character of the operation R_e in the IR r and we sum over all the elements of a certain IR. The projection operator gives 4 single electron orbitals which transform according to the symmetry operation (more precisely-IR) of the C_{3v} group [16]:

$$\begin{cases} a_N = \sigma_1 \\ a_c = \frac{\sigma_2+\sigma_3+\sigma_4}{3} \\ e_x = \frac{2\sigma_2-\sigma_3-\sigma_4}{\sqrt{6}} \\ e_y = \frac{\sigma_3-\sigma_4}{\sqrt{2}} \end{cases} \tag{1.4}$$

The first two orbitals are totally symmetric and we say that they transform as A_1 IR. The $e_{x,y}$ orbitals transform as the E IR to give a spatial doublet. Via Coulomb interaction, the totally symmetric orbitals are mixed [17] and we obtain a final basis $\{a_1', a_1, e_x, e_y\}$ where

$$\begin{cases} a_1' = \sqrt{1-\alpha^2}\sigma_1 - \frac{\alpha}{\sqrt{3}}(\sigma_2+\sigma_3+\sigma_4) \\ a_1 = \alpha\sigma_1 - \sqrt{\frac{\alpha}{3}}(\sigma_2+\sigma_3+\sigma_4) \end{cases} \tag{1.5}$$

where α describes the amount of mixing with $0 \le \alpha \le 1$ and the e_x and e_y stay the same. The orbitals can be ordered energetically from top to bottom: $e_{x,y}, a_1, a_1'$. The lowest level, a_1', is completely filled and positioned below the valence band (while the other levels are well inside the energy gap) and will not be taken into consideration in our optical or MW excitation-decay

cycles [17]. When the system is in its ground state, the orbital a_1 is also completely filled and we have two electrons occupying each of the $e_{x,y}$ states (according to the Aufbau principle) as depicted in Fig. 1.2. Therefore, ignoring the a_1' level, the ground state has the configuration of $a_1^2e^2$ (or just e^2) where the superscript stands for the number of electrons in that level. We have two electrons in a_1 and one electron in each e state, and if we excite one electron, we will go to the $a_1^1e^3$ configuration (or just ae).

For a full description of the system we need to take into account all the 6 electrons, but in order to reduce complexity, it is very common to consider a 2-hole model [1] and calculate the eigenfunctions once again using the projection operator

$$\psi_r = \frac{l_r}{h}\sum_e \chi_e^r R_e\phi_1 R_e\phi_2\,, \tag{1.6}$$

where $\phi_{1,2}$ are the single orbital functions. Each electron has spin one-half, and a 2-hole system will yield singlet and triplet states. When we assign spin to the different spatial states that we presented, we finally get a full description of all possible wave functions with respect to both the spatial and spin parts, which can be found in Table 1.3.

In order to further classify the wave function of the system, we inspect the total wave function. We note that it can be separated into a spatial part that will have a certain symmetry as discussed above, as well as a spin part $\Psi_r = \psi_r\Phi_S$ where ψ_r is taken from Eq. (1.6) and Φ_S is the spin part that can be a spin singlet ($S = 0$) or triplet ($S = 1$). According to the first Hund rule, the two spins of the ground state are co-aligned, therefore the ground state is a spin triplet. In addition the Pauli principle requires that the total wave function, Ψ_r, must be anti-symmetric with respect to exchange of particles, and since the spin part of the ground state is symmetric (triplet), the spatial part must be anti-symmetric. This eliminates the possibility for A_1 symmetry. The degenerate E symmetry is unstable and cannot represent a ground state. Hence the ground state must have A_2 symmetry. We mark the fact that it is also a spin triplet by adding an superscript ${}^3A_2$. The excited state is also a triplet and we denote it by ${}^3E$. For better understanding, we illustrate in Fig. 1.2 an example of the configuration that gives the $m_s = -1$ spin projection.

Electronic Configuration	c_{3v} Symmetry	Wave Function	m_s
e^2(T)	${}^3A_2$	$\|e_xe_y - e_xe_y\rangle \otimes \|\uparrow\downarrow + \downarrow\uparrow\rangle$	0
		$\|e_xe_y - e_ye_x\rangle \otimes \|\downarrow\downarrow + \downarrow\downarrow\rangle$	-1
		$\|e_xe_y - e_ye_x\rangle \otimes \|\uparrow\uparrow + \uparrow\uparrow\rangle$	+1
e^2(S)	${}^1E$	$\|e_xe_x - e_ye_y\rangle \otimes \|\uparrow\downarrow - \downarrow\uparrow\rangle$	0
		$\|e_xe_y + e_ye_x\rangle \otimes \|\downarrow\downarrow + \downarrow\downarrow\rangle$	0
	${}^1A_1$	$\|e_xe_x + e_ye_y\rangle \otimes \|\uparrow\uparrow + \uparrow\uparrow\rangle$	0
$ae(T)$	${}^3E$	$\|a_1e_x - e_xa_1\rangle \otimes \|\uparrow\downarrow + \downarrow\uparrow\rangle$	0
		$\|a_1e_x\rangle \otimes \|\downarrow\downarrow + \downarrow\downarrow\rangle$	-1
		$\|a_1e_x\rangle \otimes \|\uparrow\uparrow + \uparrow\uparrow\rangle$	+1
		$\|a_1e_y + e_ya_1\rangle \otimes \|\uparrow\downarrow - \downarrow\uparrow\rangle$	0
		$\|a_1e_y\rangle \otimes \|\downarrow\downarrow + \downarrow\downarrow\rangle$	-1
		$\|a_1e_y\rangle \otimes \|\uparrow\uparrow + \uparrow\uparrow\rangle$	+1
ae(S)	${}^1E$	$\|a_1e_x + e_xa_1\rangle \otimes \|\uparrow\downarrow - \downarrow\uparrow\rangle$	0
		$\|a_1e_y + e_ya_1\rangle \otimes \|\uparrow\downarrow - \downarrow\uparrow\rangle$	0

Table 1.3: Wave-functions of the NV system. The letters T and S in the brackets stand for triplet and singlet states respectively. The electronic configuration e^2 is the optical ground state and ae is the optical excited state. In the thesis we will focus mainly on the triplet states that serve as our ground and excited states in the optical excitation-emission cycle and on the magnetic sub-levels of the ${}^3A_2$ state.

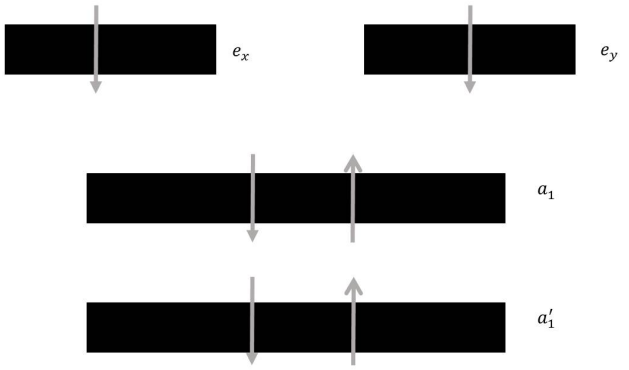

(a) Example of the ground state level configuration. a_1' and a_1 levels are completely filled and the wave function is $|e_x e_y\rangle = |^3A_2\rangle$ with total spin number of $m_s = -1$.

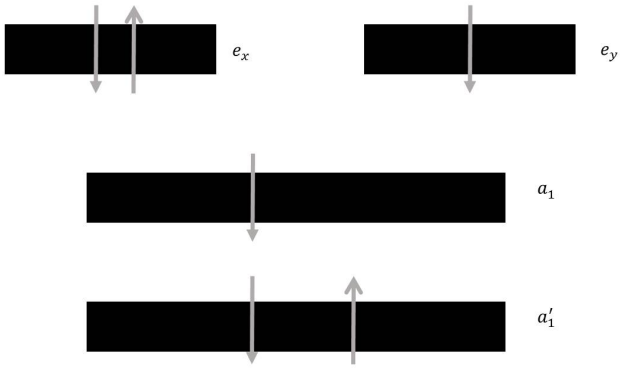

(b) Example of the ground state level configuration. a_1' is completely filled. The wave function is $|a_1 e_y\rangle = |^3E_y\rangle$ with a total spin number of $m_s = -1$.

Figure 1.2

1.3 Electric Dipole Transitions

The optically excited state (ES) is a spin triplet and also a spatial doublet that transforms as the E IR. The optical ground state (GS) is also a spin triplet but its spatial part transforms as the A_2 IR. At room temperature the orbital doublet of E is said to "average out" [18] to form a spatial singlet and spin triplet.

Starting in the GS, we can access the ES using a green laser via dipole interaction. In order to have a non-zero possibility for a dipole transition, the system must obey the following equation:

$$\langle \Psi_f | d \cdot \mathbf{E} | \Psi_i \rangle \neq 0 \,, \tag{1.7}$$

where Ψ_i (Ψ_f) is the initial (final) state, d is the electric dipole operator and $\mathbf{E}$ is the electric field. We can understand why Eq. (1.7) does not equal zero by applying symmetry considerations. We can replace the dipole operator, d, with the position operator, r, as they are proportional, and work with the position operator. Due to the C_{3v} structure of our system, z which is the symmetry axis of the structure transform as the A_1 IR and x and y transform as the E IR. We also know that the GS transforms as A_2 and ES transforms as E. Putting all this together in Eq. (1.7), we find allowed transitions only if $d \cdot E$ transform as the E IR. Thus we conclude that if the electric field

is polarized along the z axis then the probability for dipole transition is zero as the dot product yields a vector along the z axis, so $d \cdot E$ transforms as A_1. But for x or y polarized light we get a non-zero probability for dipole transition.

The electric dipole process only operates on the spatial part of the wave function and leaves the spin part unchanged. Therefore, unless there is a perturbation that mixes the states such as spin-orbit coupling, the process is spin conservative.

1.4 Energy Levels

1.4.1 The Ground State Hamiltonian

The optical ground state (GS) is a spin triplet and spatial singlet that transforms as A_2. The full Hamiltonian of the GS is:

$$\begin{cases} \mathcal{H}_{\mathcal{S}} = D_{\text{gs}} S_z^2 + g_s \mu_B (\mathbf{B} \cdot \mathbf{S}) + E(S_y^2 - S_x^2) \\ \mathcal{H}_{\mathcal{I}} = P I_z^2 - g_I \mu_N (\mathbf{I} \cdot \mathbf{B}) \\ \mathcal{H}_{\mathcal{SI}} = A(\mathbf{S} \cdot \mathbf{I}) \end{cases} \tag{1.8}$$

The $\mathcal{H}_{\mathcal{S}}$ Hamiltonian stands for the spin Hamiltonian, H_I for the nuclear Hamiltonian and H_{SI} describes the interaction of the nuclear spins with the electronic spins. The electronic spin in NVs is $S = 1$ and also the nuclear spin is $I = 1$ as we take into account only the nucleus of the nitrogen which is $I = 1$ (as the natural abundance of ^{14}N, which has a spin 1, is 99.6 %, unless special treatment is performed to the diamond). In this thesis we will assume that the carbon atoms are ^{12}C and therefore will not consider any other nuclear spins except of the nitrogen atom in the NV structure although ^{13}C or ^{14}N defects can be taken into consideration as noise or a dephasing source, and there are several ways to eliminate or reduce their effect [19].

Looking at the spin Hamiltonian, the axial spin-spin interaction, described by the $D_{\text{gs}} S_z^2$ term, destroys the triplet degeneracy, where $D_{\text{gs}} \simeq 2.87\,\text{GHz}$, so both $m_s = \pm 1$ states differ equally from the $m_s = 0$ state. This is also known as the zero-field splitting (ZFS). The degeneracy is then completely removed by the transverse spin-spin interaction, which can be considered as strain fields [20] that break the degeneracy of the $m_s = \pm 1$ state and yield a $2E$ separation between the new states. The amplitude of the strain ranges from several hundred kHz (in CVD diamonds) up to few MHz (in HPHT diamonds) [5]. An additional external field along the z quantum axis will further push the spin levels away by a factor of 2.8 MHz/G as the Landé factor is $g_s = 2.003$ and $\mu_B = 1.4\,\text{MHz/g}$ is the Bohr magneton. Note, as described in Fig. 1.1a, that there are 4 possible NV orientations, and therefore 4 different quantum axes as the z quantum axis is defined by the nitrogen vacancy axis, and an external field that is aligned with one orientation is at 109° relative to the other 3 z quantum axes. Thus, the magnetic field that the other three orientations feel along their local z axis is $B\cos(109°)$. The effect of four NV orientations on the atomic spectrum in the presence of an external magnetic field will be discussed in Ch. 3

The spin-1 nuclear system generates a spin-spin interaction which can be described by PI_z^2 where $P = -4.95\,\text{MHz}$. The nuclear spin also interacts with the external magnetic field. However this interaction is very weak, almost 2000 times weaker than the interaction of the electronic spin with the magnetic field, as the nuclear magnetic moment is $\mu_N = 0.76\,\text{kHz/G}$ and $g_I = -0.416$. In this thesis, where we use magnetic fields of no more than a few dozen Gauss and no less than 1 kHz resolution, it can be neglected.

Finally, the HF Hamiltonian which describes the interaction of the nuclear spin with the electronic spin can be rearranged as

$$\mathcal{H}_{\mathcal{SI}} = A_{\parallel} S_z I_z + A_{\perp}(S_x I_x + s_y I_y) \tag{1.9}$$

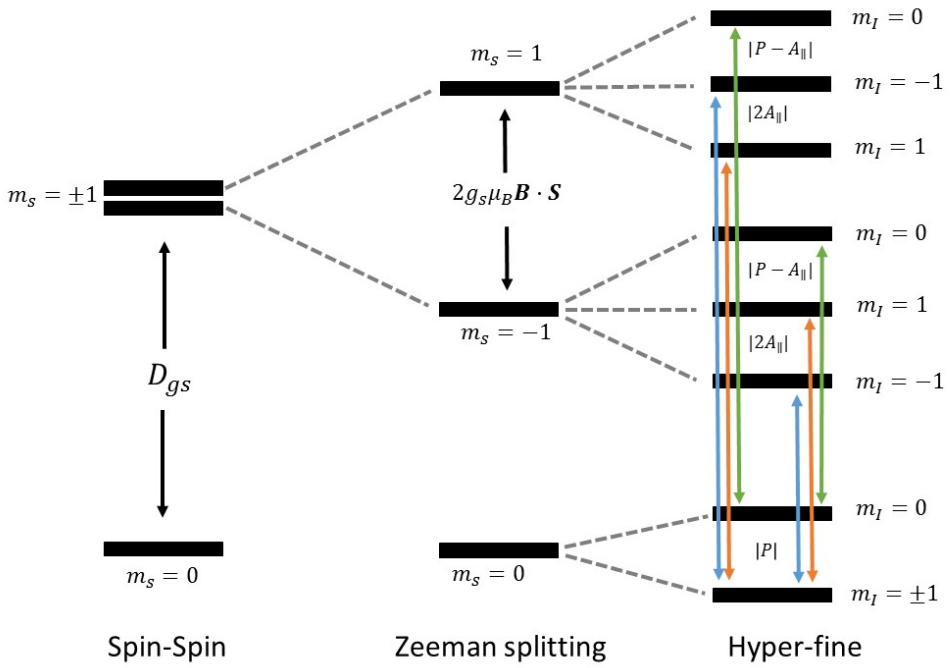

Figure 1.3: Ground state energy levels and allowed transitions. The green line shows a MW transition from $|m_s = 0; m_I = 0\rangle$ to $|m_s = \pm 1; m_I = 0\rangle$. The blue and orange lines show a similar transition but with $m_I = -1$ and $m_I = 1$ respectively.

where $A_\perp \approx 2.7\,\text{MHz}$ and $A_\parallel \approx 2.16\,\text{MHz}$. The ^{14}N nuclei with its $\mathbf{I} = 1$ causes a 3-fold splitting in each of the Zeeman levels giving rise to a 9-state system, and the allowed MW transition ($\Delta m_s = \pm 1$), as depicted in Fig. 1.3, conserves the nuclear angular momentum projection ($\Delta m_I = 0$).

1.4.2 Level Crossing and Polarization

During the time that the system is in the excited state ($\sim 10\,\text{ns}$), there is a low mixing (at room temperature) among the different m_s levels [18] but the decay process, in contrast, does not necessarily conserve the projection of the spin.

In order to understand why the decay is not spin conserving, we need to take a closer look at the entire process. We start by introducing phonon coupling and vibronic levels to each optical state. The energy difference between the ground and excited states' lowest vibronic levels is 637 nm, also known as zero phonon line (ZPL). The phonon coupling generates a continuous absorption and emission spectrum and in addition also changes the most probable transition frequency from ZPL to $\sim 580\,\text{nm}$ due to the Frank-Condon effect. Therefore when we excite the system it goes to a vibrational excited level from which it decays very fast ($\sim$ ps) to the lowest vibrational level in the excited states. This fast vibrational level decay conserves spin and even phase. The wide absorption band near 580 nm makes the commonly used 532 nm green laser a good choice for excitation; not only is this laser common, inexpensive and efficient, it can also help distinguish between excitation light (green) and emission light (red).

After the system stays in the excited state roughly 10 ns it can decay back to the ground state in two ways: a) it can decay directly to the ground state with $\Delta m_s = 0$ as expected, while emitting a red photon in the process, or b) it can decay non-radiatively to an intermediate singlet level ($^1A_1$) and decay radiatively (1042 nm) within 1 ns lifetime [21] to another singlet level (^1E) [22] where it stays roughly 200 ns before it decays phonon-like with (roughly) equal probabilities to the $m_s = 0$ and $m_s = \pm 1$ ground states [23].

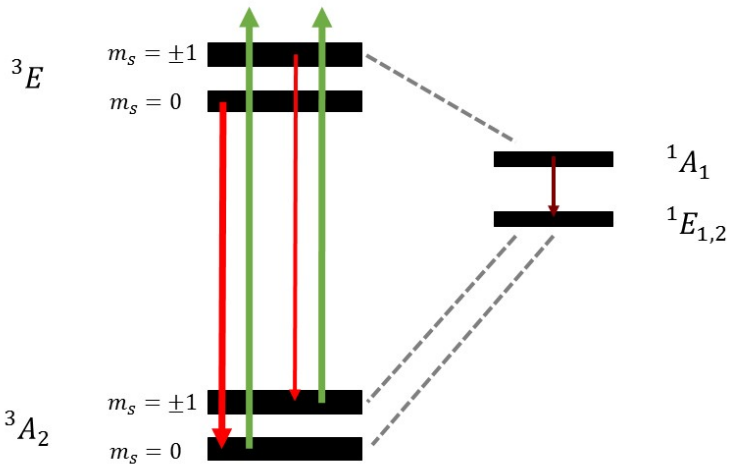

Figure 1.4: Intersystem crossing. Optical (non-radiative) transitions indicated by solid (dashed) lines. The green line represents optical excitation to an excited vibrational level of the ^3E state. After a fast phonon decay to the vibrational ground state in ^3E, the system can go to the GS through a radiative decay which is indicated by red arrows, or it can decay non-radiatively to the $^1A_1$ singlet level. From the $^1A_1$ level it decays to the other singlet level, ^1E (indicated by the dark red line of 1042 nm). From ^1E the system decays again non-radiatively to the $m_s = 0$ and $m_s = \pm 1$ ground state levels with equal probabilities. The red line for the optical decay to $m_s = 0$ is thicker than that for the decay to $m_s = \pm 1$ to emphasize that this path a has higher rate of fluorescence .

The path through the singlet levels is possible due to spin-orbit coupling in the excited state: the sub-states of the ^3E state that have a non-zero spin projection number can have a first- (and also second-) order spin-orbit transition to a $^1A_1$ vibrational level so the spin-orbit coupling induces transition between the states while changing from triplet state to singlet [22]. Hence, the decay path through the singlet level is more preferable for the excited $m_s = \pm 1$ states than for the excited $m_s = 0$ state. Thus, while the $m_s = 0$ state has a spin conserving excitation-decay cycle, the $m_s = \pm 1$ can end up in the $m_s = 0$ ground state. The net effect of this process is polarization into the $m_s = 0$ ground state after a few cycles. In addition to this very efficient initialization into a specific quantum state, the decay through the dark channel can also allow us to distinguish between the different quantum levels easily, as the $m_s = \pm 1$ has a reduced emission rate compared to the $m_s = 0$ state.

Finally, let us note that because of the high occupancy of vibrational states at room temperature, only a few percent of the emitted photons are at 637 nm. Most of the emission spectrum is spread along the near infra-red over hundreds of nano-meters (Fig. 1.5).

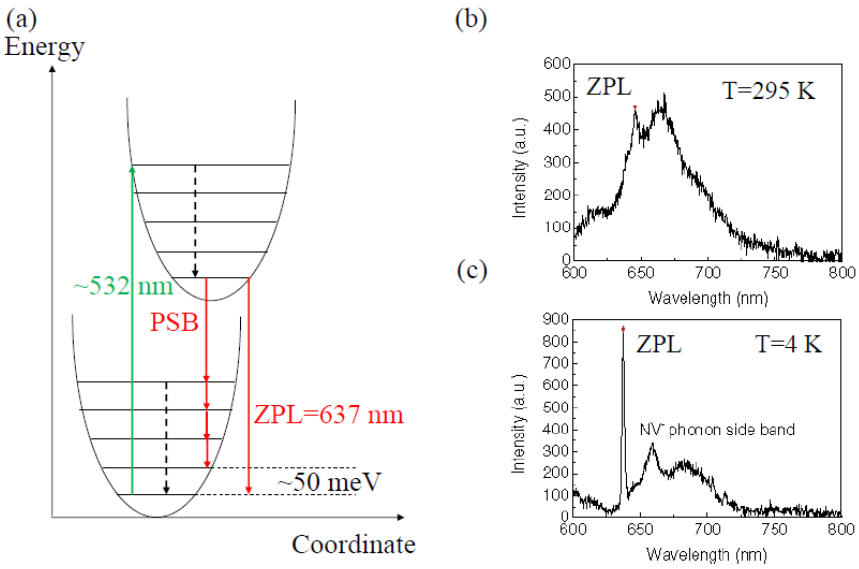

Figure 1.5: (a) Illustration of the Franck Condon rule via a schematic of the NV system excitation and emission cycle. The most probable transition is indicated by a green arrow. The non-radiative decay is denoted by dashed arrow, while the radiative decay is indicated by a red arrow. (b-c) Photoluminescence spectra of the NV centers at room temperature (b) and at 4 K (c). Figure taken from [1].

Chapter 2

Experimental Setup

In general, at the heart of an NV experimental setup there is a green laser to excite and polarize the NVs (i.e., prepare the system in a quantum state), an MW antenna to manipulate the system between the different quantum states, and a detector to collect the emitted photons which could tell us what the state is. On top of that we can add different optics tools or MW equipment, depending on the needs of the experiment. In this chapter we explain the experimental setup that was constructed. A schematic diagram of the experimental setup appears in Fig. 2.1.

In order to excite and polarize the diamond (as explained in Sec. 1.4.2) we work with a CW 532 nm solid state laser with ~ 100 mW output power. The laser is aligned using mirrors, and by adding a half-wave plate (HWP) and a polarizing beam splitter (PBS), we fully polarize the beam parallel to the table plane and perpendicular to the beam propagation direction so the beam does not reflect when it enters the PBS.

Once we set the beam polarization according to the PBS, the beam enters a double pass acousto-optics modulator (AOM) setup that serve as an optical switch. The AOM (Crystal Technology, 3080-125) has an AOM driver (Crystal Technology, 1080AF) that generates acoustic waves at 80 MHz inside the AOM crystal, which interact with the laser to create a diffraction pattern. We insert an iris in order to choose only the +1 diffraction order, and block all other orders. After the iris we position a quarter-wave plate (QWP) and a mirror that reflects the +1 order back through the iris into the AOM and to the PBS, except that now the laser has a 90° rotation in the polarization as the beam passes twice through the QWP. Therefore, the outgoing beam will now reflect from the PBS and up to the rest of the optical setup, and will not pass through the PBS as the ingoing beam. The AOM driver can be modulated on-off with a nano-second resolution using modulated low-voltage high-voltage signals (also known as a TTL signal where low voltage is typically $0-0.8$ V and high voltage is $2-5$ V) generated by Pulse Blaster ESR-PRO 500 MHz. When we give the driver low voltage, the driver is off and there is no diffraction pattern, thus the laser (i.e., zero order) hits the iris and is absorbed. When the AOM driver is on, there is a diffraction pattern and the +1 order goes through the iris and back to the AOM and PBS and continues to the rest of the optical path. Thus we can effectively modulate the laser on-off with a resolution of 1 μs and better. We installed this option for a future application that will be discussed in App. C. However for the experiments presented in this thesis, we did not use this option and the TTL operated at a constant high-voltage. The entire double-pass AOM setup reduced the laser intensity to 30mW, as measured after reflection from the PBS. Further elaboration regarding the principles of AOM and a double-pass optical switch setup can be found in App. A.

Following the optical switch AOM setup, the laser is realigned using mirrors, and hits a long-pass dichroic mirror that reflects the laser into a microscopic objective (Olympus, Pro-Plan 40× magnification; N.A.=0.6) which focuses the green light to a spot size on the surface of a [1 1 1] HPHT diamond. The green light excites the NV and after 10 ns a red photon is emitted in the decay process, as explained in Sec. 1.4.2. The same objective then collects the emitted light, which

now can pass through the dichroic mirror as it now has a longer wavelength. The fluorescence hits a fast avalanche photo-diode (ThorLabs, APD110A). In order to measure the voltage that the fluorescence light generates in the photo-diode, we connected the photo-diode to a lock-in amplifier.

The lock-in amplifier has the following general working principle: assume that the signal has the form of $V_s \sin(\omega_s + \theta_s)$ and a reference signal that goes as $V_r \sin(\omega_r + \theta_r)$. Using a mixer, we multiply the signal with the reference. If we assume that $\omega_s = \omega_r$ then with a little trigonometry we obtain for the mixer output

$$V_{mix} = \frac{1}{2} V_r V_s (\cos \Delta\theta + \sin(2\omega_r + \Theta)) \,, \tag{2.1}$$

where $\Delta\theta = \theta_r - \theta_s$ and $\Theta = \theta_r + \theta_s$. A low-pass filter is used to eliminate the sine term and we are left with $V_{mix+filt} = \frac{1}{2} V_r V_s \cos \Delta\theta$. By using a splitter and a phase shifter, we can get another signal: $V'_{mix+filt} = \frac{1}{2} V_r V_s \sin \Delta\theta$. Different types of manipulation can be done on $V_{mix+filt}$ and $V'_{mix+filt}$ to give different insights regarding the measured data, such as the "in-phase" component, "quadrature" component, etc. We choose to work with the amplitude component:

$$R = \sqrt{2} V_s \,, \tag{2.2}$$

where the cosine and sine terms vanish using trigonometry and the fact that they have the same argument. The voltage that the photo-diode generates in response to the fluorescence light could have also been measured using a simple oscilloscope, but since for this thesis the fluorescence was modulated at a certain frequency, as a consequence the voltage of the photo-diode had the same modulation rate. Thus, working with a look-in was a much more natural choice than an oscilloscope. The reference signal was generated using the pulse-blaster and was connected, together with the photo-diode signal, to either a EG&G 7260 slow lock-in amplifier (slow setup) or to an SR844 fast lock-in amplifier (fast setup).

In the slow setup we used 2 different permanent magnets. One of these magnets was later used in the fast setup, so we had a total of 3 different setups. When switching between all 3 setups (i.e slow using two different magnets and fast) we realigned the laser, which caused a $2-3\,\mathrm{mW}$ deviation in laser power between setups. When we switched from the slow lock-in to the fast lock-in, we did not touch the permanent magnet, but we did do a realignment of the laser which could result in a $2-3\,\mathrm{MHz}$ deviation in resonance frequency due to the magnetic field gradient. There was also a change in the NV resonance frequency between the two slow setups since the two magnets had different amplitudes and were placed at different locations. In addition, the location of the green laser on the diamond moved by a few microns between each setup. The magnet that was later used for the fast setup was placed in such a way that the effective magnetic field was along the [1 1 1] direction, while the other magnet was placed in an arbitrary direction.

Excitation of the ground state MW transition levels was done using a home-made micro-strip antenna that was fed by two MW signals: a pump MW signal, generated by R&D SMR20 and a probe signal generated using SRS SG384. Both pump and probe were operating in CW mode, except that the pump signal was modulated using a MW shutter (Mini-Circuits, ZASWA-2-50DR+), and both fields (modulated pump and CW probe) were then combined using a Mini-Circuits' ZB4PD-42 beam combiner. Following combination, the sum was fed into an amplifier (Mini-circuits ZHL16W-43+) and the amplifier output was connected to the antenna. The modulation of the pump, 36.6 kHz in fast setup and 426 Hz in the slow setup, was controlled using the fast pulse generator. The pulse generator also gave the modulation signal to the lock-in and we chose the reference to be identical to the MW modulation signal of the pump, as the fluorescence is expected to oscillate at the same frequency as the reference signal.

We connected all the instruments to the same computer and using a LabView program we could control all the instruments and retrieve the signal from the lock-in as a function of MW amplitude, modulation rate, etc.

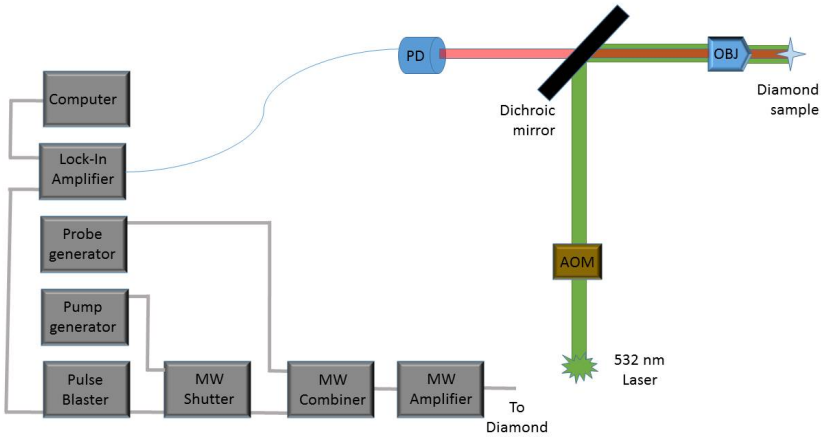

Figure 2.1: Schematic diagram of the experimental setup. Right: the laser passes through the double pass AOM setup (AOM) and hits a dichroic mirror. The reflected beam is focused by an objective lens (OBJ) into the diamond and the fluorescence passes through the OBJ and dichroic mirror and is collected by the photo-diode (PD) with its output connected to a lock-in amplifier. Left: the MW pump generator is connected to a MW shutter which modulates the signal, and then the pump signal is combined with the MW probe signal. The combined signal is amplified and the total amplified signal (modulated pump and CW probe) is injected into a MW antenna near the diamond. The modulation rate of the MW shutter is controlled by a pulse generator that also gives the reference for the lock-in amplifier. All instruments are connected to the same computer and can be controlled remotely.

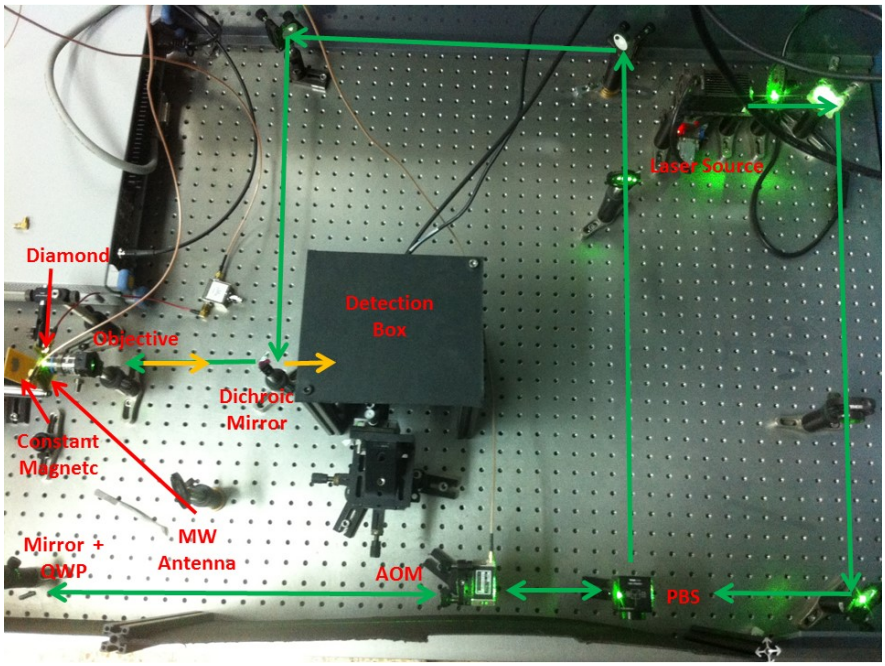

Figure 2.2: Optical table setup. Green arrows- path of green laser. Yellow arrow above green arrow- the path of fluorescence light after the objective. The double-head green arrows before and after the AOM represent laser light that enters and gets out of the AOM setup (for explanation see App. A). The laser that comes out of the AOM, enters again the PBS, reflects and proceed to the rest of the optical setup.

Chapter 3

Standard ODMR and Magnetic Sensitivity

In this Chapter, we explain and present the ODMR technique and show how to derive from it the relation between the NV magnetic sensitivity and the transition linewidth. We also show how the sensitivity of the ODMR changes with the MW power, and use this result to choose the most suitable MW power for our experiment.

3.1 Introduction

In an ODMR experiment, we detect a magnetic resonance transition using optical changes (absorption, fluorescence, etc.). As explained in Sec. 1.4.2, we expect a change in the fluorescence rate coming out of the diamond with a transition from $m_s = 0$ to $m_s = \pm 1$ (ground states), as once excited by a green laser the $m_s = 0$ should shine brighter than $m_s = \pm 1$ state, since the excited $m_s = 0$ does not partially decay through a non-radiative "dark" channel and thus has a higher rate of fluorescence photons.

During an ODMR experiment, we shine a CW green light on the diamond and this polarizes the system into the $m_s = 0$ state. In addition, we scan with a MW field and monitor the relative fluorescence as a function of the MW field frequency. If there is no external magnetic field, we expect to see a reduction in the fluorescence rate at 2.87 GHz when the MW induces a transition to the $m_s = \pm 1$ states. An external magnetic field will split the Zeeman levels and the resonance levels will have different frequencies. We can evaluate the amplitude of the magnetic field by scanning with a MW field until we see a reduction in fluorescence at a certain MW frequency and consequently retrieve the magnetic field amplitude.

This picture gets a little more complicated when we introduce all 4 different NV orientations in the diamond crystal. The dot product between $\mathbf{B}$ and $\mathbf{S}$ in the Hamiltonian forces us to take into consideration both axial and transverse magnetic fields. For example, applying an external magnetic field along one NV axis (which is also the z quantum axis of that orientation) will yield four spectroscopic transitions. Two of them are the $m_s = \pm 1$ transition frequencies of the NV orientation that is aligned with the magnetic field, and the other two are associated with the $m_s = \pm 1$ levels of the other 3 orientations as they all sense the same magnetic field at the same angle relative to their local z axis (109°). In this simple case we can retrieve the magnetic field amplitude by dividing the frequency difference of the magnetic levels of the aligned orientation from 2.87 GHz by 2.8 MHz/G. The typical situation is, however, that all 4 orientations have slightly different magnetic field projections and we thus have as many as 8 different transitions. For this general case, we need to insert the non-axial terms in $\mathcal{H}_S$, $B_x S_x$ and $B_y S_y$ with respect to each orientation's local quantum axis. This complexity has also an up side as it enables us to sense not

only the field's magnitude but also its orientation [24] thus having a full description of the magnetic field.

3.2 Magnetic Sensitivity

Let us assume that we apply only the laser radiation. The green laser polarizes the system into state $m_s = 0$ which is the brightest m_s state and has a certain red photon emission rate, R. When we start an ODMR scan we apply a MW field with frequency (at first) far from resonance, ν_0, so it does not change the photon rate. As we bring the MW frequency, ν, closer to resonance, there will be some population transfer into one of the other m_s states that has a reduced photon rate. This will cause a reduction in the fluorescence intensity. Therefore we can say that the signal will take the form $S(\nu - \nu_0)$. Assuming a Lorentzian shape for the ODMR (i.e. the reduction in signal as a function of $\nu - \nu_0$), we obtain a general description of the ODMR signal [25]:

$$S(\nu - \nu_0) = R\Big(1 - \frac{C(\Delta\nu/2)^2}{(\nu - \nu_0)^2 + (\Delta\nu)^2}\Big)\,, \tag{3.1}$$

where $\Delta\nu$ and C are the transition FWHM and amplitude respectively.

The largest change in the signal with respect to a change in ν will be where the slope of the Lorentzian is highest:

$$max\left|\frac{\partial S}{\partial \nu}\right| = \frac{RC}{\Delta\nu\alpha}\,, \tag{3.2}$$

where $\alpha = 0.77$ is a numerical value which is related to our choice of a Lorentzian line shape [26] (if we had chosen a Gaussian shape, then the value of α would be 0.7). If we assume that C is very small, then the number of collected photons β, during a measurement time of δt_m, will be $\beta \simeq Rt_m$, and the corresponding photon shot noise will be $\delta\beta = \sqrt{R\delta t_m}$. We can estimate the minimum detectable magnetic field as [27]:

$$\gamma\delta B_{min} = \Delta\nu_{min} = \frac{\delta\beta}{max\left|\frac{\partial\beta}{\partial\nu}\right|} \simeq \frac{\sqrt{Rt_m}}{t_m max\left|\frac{\partial S}{\partial\nu}\right|}\,, \tag{3.3}$$

where $\gamma = g_s\mu_B/h$ transforms magnetic field to frequency as shown in Ch. 1. The value of $max\left|\frac{\partial\beta}{\partial\nu}\right|$ is about equal to $t_m \times max\left|\frac{\partial S}{\partial\nu}\right|$ because under the assumption of low C, $S \simeq R$. Substituting Eq. (3.2) into Eq. (3.3) yields:

$$\delta B_{min} = \alpha\frac{h}{g_s\mu_B}\frac{\Delta\nu}{C\sqrt{Rt_m}}\,. \tag{3.4}$$

It is customary to describe the sensitivity not as δB_{min} but as [28]:

$$\eta = \delta B_{min}\sqrt{t_m}\,. \tag{3.5}$$

The parameters of the sensitivity are not completely independent. For example, increasing MW power will increase C but will also increase $\Delta\nu$. These parameters can be optimized [26] to give maximum sensitivity. This can be done using a Ramsey sequence. In the Ramsey sequence we prepare the system in state $|0\rangle$ using green light. Then we turn off the green light and apply the following MW pulses: $\frac{\pi}{2} - \tau - \frac{\pi}{2}$. The first $\frac{\pi}{2}$ takes state $|0\rangle$ into a coherent superposition $\frac{1}{\sqrt{2}}(|0\rangle + |1\rangle)$. Then we wait for time τ without any laser or MW fields. During the waiting time the magnetic level interacts with the external magnetic field and accumulates a relative phase, $\phi = \tau g_s\mu_B B/\hbar$, compared to state $|0\rangle$. A final MW pulse $\frac{\pi}{2}$ projects the spin state $\frac{1}{\sqrt{2}}(|0\rangle + e^{i\phi}|1\rangle)$

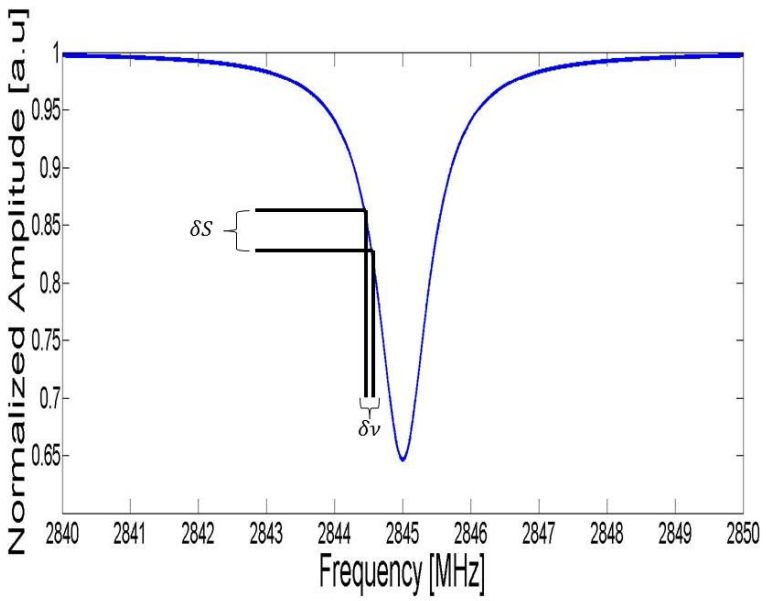

Figure 3.1: Magnetic sensitivity. At the highest slope of a Lorentzian, a small change in the frequency, $\delta\nu$, causes a large corresponding change in the signal, δS. If that small change in frequency originates from an additional magnetic field, we can evaluate that additional field according to the relative change in the signal.

back into the quantization axis and the additional phase may be detected as population difference [29] and the magnetic field can be retrieved. Once the MW sequence is done, we apply a green light for population read out. This process is limited by the inhomogeneity of the ensemble introducing a dephasing time characterized by T_2^*. The process can be optimized by setting $\tau = T_2^*$ [29] and the optimized sensitivity will be:

$$\eta = \alpha \frac{2\hbar}{g_s \mu_B} \frac{1}{C\sqrt{\beta T_2^*}}\,, \tag{3.6}$$

where β describes the amount of photons emitted when the system is in $m_s = 0$. Therefore, when we have an ensemble of NVs, β will grow linearly with the numbers of emitters, N. If we will use the FWHM sign, Γ, instead of T_2^* (i.e., $\Gamma = 2\pi/T_2^*$) we can see that the sensitivity of the system is:

$$\eta \propto \sqrt{\frac{\Gamma}{N}}\,. \tag{3.7}$$

It is clear that if we are interested in magnetic sensing, there is great significance in the width of the transition line. When we are using an ensemble of NVs, the transition width has several line broadening mechanisms. Some occur in single NV measurement as well. These include: natural linewidth, power broadening due to the MW field, etc. Others are solely related to ensemble effects such as inhomogeneity that can arise from local fields as well as the gradient of an external field. A complete description of the line broadening in an ODMR experiment can be shown to be [25]:

$$\Delta\nu_{tot} = \Delta_{inh} + \Delta\nu\,, \tag{3.8}$$

where $\Delta_{inh} = \frac{1}{\pi T_2^*}$ is the inhomogeneous broadening arising from an ensemble measurement and

$$\Delta\nu = \sqrt{(\frac{1}{\pi T_2^{eff}})^2 + (\frac{4T_1^{eff}}{T_2^{eff}})}\,, \tag{3.9}$$

is true for single NV measurement as well, where T_1^{eff} and T_2^{eff} are the longitudinal and transverse relaxation times respectively. We donated the eff superscript to symbolize the fact that we take into account the influence of the continuous pumping into $m_s = 0$ state due to the CW green laser, as we do in an ODMR measurement.

To conclude, the sensitivity of measuring a magnetic field using the ODMR technique (as well as other techniques) has a basic limit as the sensitivity is proportional to $\sqrt{\Gamma/N}$, where Γ is the spectroscopic linewidth and N is the number of centers being probed. The relation between Γ and N is somewhat entangled, since an increase in the number of NVs being probed will cause line broadening in the form of inhomogeneous broadening due to the different local fields at each single NV environment (e.g. MW fields, magnetic fields, strain fields, etc.). In this thesis we introduce a new spectroscopic method that has a narrower linewidth compared to the ODMR technique (to the kHz regime) that might prove useful in sensitive measurements as well as enabling more insight into the origins of the inhomogeneous broadening.

3.3 MW Calibration

We began the calibration of the MW by placing a permanent magnet near the diamond in such a way that the effective field of the magnet is along the [1 1 1] axis which is one of the NV axes. If we indeed placed it properly, we expect to see only 4 MW transitions in our ODMR spectrum. Two of the transitions are associated with $m_s = \pm 1$ Zeeman levels of the [1 1 1] orientation, and the other two are associated with the Zeeman levels of the other three orientations which are degenerate as they all have the same magnetic projection. An ODMR scan (Fig. 3.2a) shows a typical spectrum of a [111] diamond and magnetic field perpendicular to the diamond surface, confirming that the magnet was placed properly.

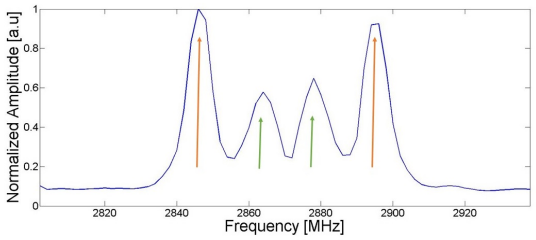

(a) ODMR using the fast setup with 0dbm MW power preamplifiaction and 2 MHz step size. The orange line represents the transition to the [1 1 1] orientation and the green line represents transitions to all other 3 orientations. This characteristic spectroscopy indicates that indeed our magnetic field is along the [1 1 1] orientation as all the other three orientations are degenerate. In this work, we focus only on the transition in the [1 1 1] orientation.

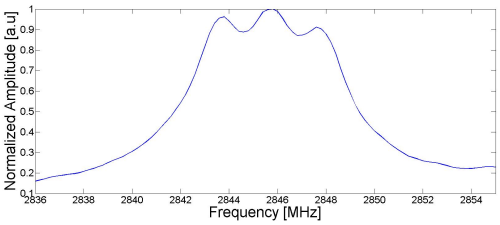

(b) Zoom-in on the extreme left transition of Fig. 3.2a most left transtion with the same setup parameters except that step size was changed to 200 kHz. The reduced step size resolved the 3 HF transitions but due to the stregnth of the MW field, the HF transition are very wide, almost 3 MHz each, but with a very high amplitude- ~ 0.8.

Figure 3.2

Now that we have placed our magnet, we want to optimize our MW power; increasing the MW power will increase the amplitude of the signal but at the cost of power broadening and therefore-reduced sensitivity. To this end, we made a series of ODMR measurements on the same m_s transition at different MW powers. For each MW power we fitted the following function:

$$fit = \sum_{i=1}^{N=3} a_i \frac{\gamma_i}{2} \frac{1}{(x - x_i)^2 + (\frac{\gamma_i}{2})} + d\,. \tag{3.10}$$

This is a fit of three Lorentzians centered at x_i with an amplitude of a_i and FWHM of γ_i that stands for each HF transition. For each MW power we calculated the mean value of the three FWHM and its estimated error:

$$\Delta\gamma = \sqrt{\Delta\gamma_i{}^2 + \frac{\sigma^2}{N}} \tag{3.11}$$

where $\Delta_{\gamma_i} = max[\gamma_1;\gamma_2;\gamma_3]$ and $\sigma = std[\gamma_1;\gamma_2;\gamma_3]$. The same calculation was done also on the

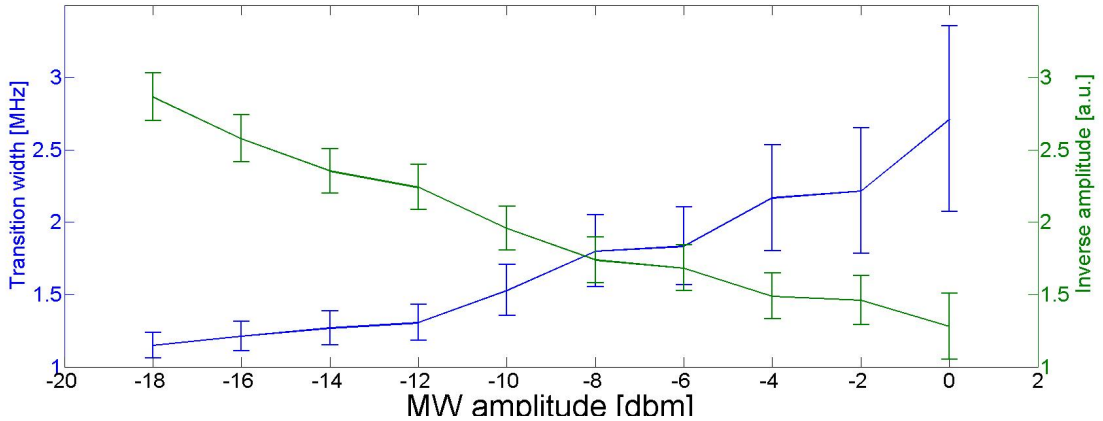

Figure 3.3: Calibration of MW power. In green we see that the inverse amplitude gets higher as we reduce the power, while on the contrary, we see how the FWHM (blue) narrows down as we do so. Starting from -12dbm, the width approaches its asymptotic value, while the inverse amplitude is roughly linear all the way. This implies that -12dbm is a good choice for the MW power.

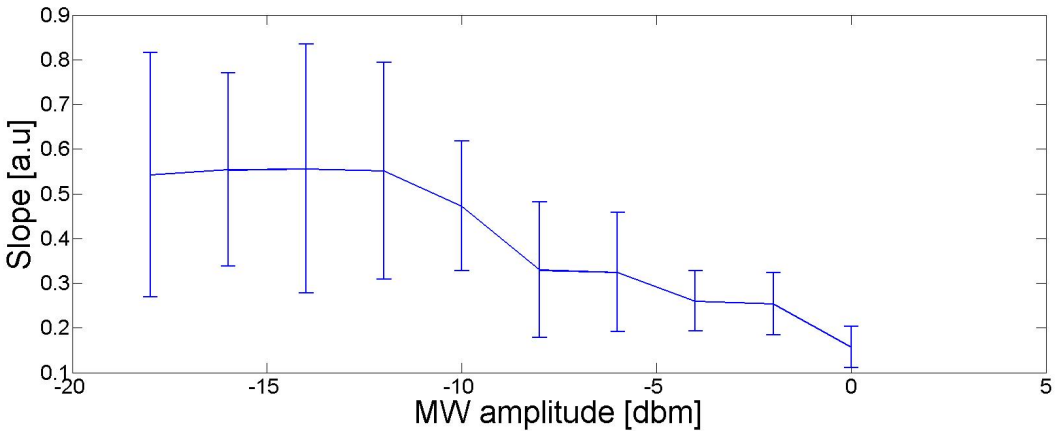

Figure 3.4: Slope vs. MW power. The higher the slope, the better the sensitivity. We can see, despite the large error, that around -12dbm we get the best slope.

amplitude a. To properly evaluate the optimum power, we generated two plots. In the first plot we plotted $1/a$ and γ vs. MW power in order to observe simultaneously the behavior of the two parameters at different powers, and next we also plotted the slope of the $m_I = 0$ transition to evaluate the sensitivity of the signal. The results, Fig. 3.3 and Fig. 3.4, show that -12dbm power is a good choice to meet our requirements for low width and high signal amplitude. Note that we could have improved the sensitivity by using lower MW power up until the power broadening is at a minimum (i.e. the linewidth will be mainly due to the homogeneous broadening), but this would initiate a time consuming process since the signal-to-noise ratio would be low, and each

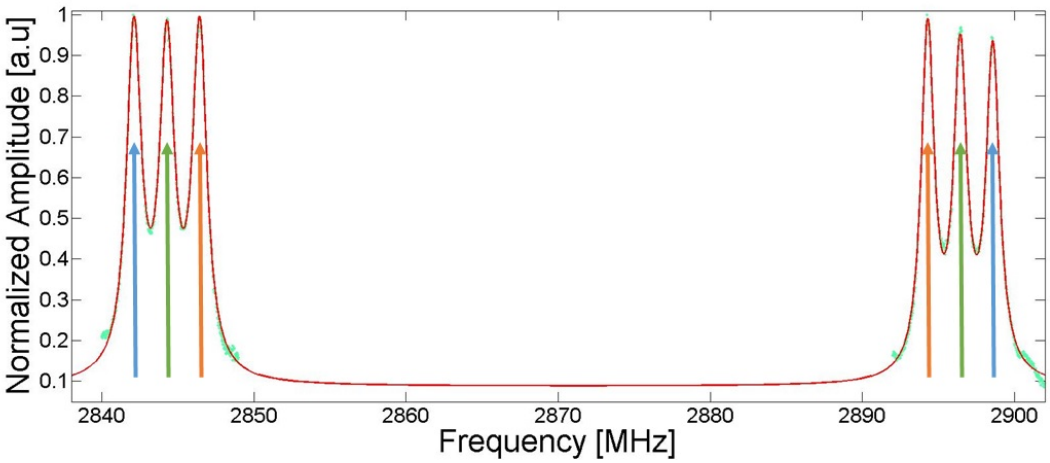

Figure 3.5: High resulotion ODMR scan of the [1 1 1] orientation with -12dbm MW power. Data in turquoise, fit of 6 Lorentzians in red. The two batches of three peaks represent the transitions from the $m_s = 0$ to the $m_s = \pm 1$ states and each color of arrow represents a transition for a different m_I state. The color code is the same as in Fig. 1.3: the blue arrows represent transitions with $m_I = -1$ nuclear spin. Green and orange lines are the transitions with $m_I = 0$ and $m_I = 1$ respectively.

measurement would need many more averages. Thus, in choosing to work with -12dbm, we also took into consideration the practical aspects of the experiment.

Chapter 4

Hole Burning Saturation Spectroscopy

In this chapter we introduce NV center saturation spectroscopy and use it to study the role of local magnetic fields in the inhomogeneous line broadening process. We will also show that the observed linewidth becomes narrower, a feature of importance for high sensitivity magnetic field measurements.

4.1 Theory

In order to achieve better understanding of NV line broadening we follow [30] and add to the Hamiltonian in Eq. (1.8) a local magnetic field δB, a local strain field $\delta\epsilon$ and neglect the nuclear spin and the strain term. The effective Hamiltonian for axial fields now reads

$$\mathcal{H} = (D_{\rm gs} + d^{\parallel}\delta\epsilon)S_z^2 + g_s\mu_B(B_z + \delta B_z)S_z\,, \tag{4.1}$$

and the transition frequencies are

$$f_{\pm} = (D_{\rm gs} + d^{\parallel}\delta\epsilon) \pm g_s\mu_B(B_z + \delta B_z)\,, \tag{4.2}$$

where $f_{\pm}$ are the transition frequencies from state $m_s = 0$ to state $m_s = \pm 1$. If we assume that the main contribution to the inhomogeneous line broadening originates from local strain fields, $d^{\parallel}\delta\epsilon$, and neglect the local magnetic field $\delta B_z \simeq 0$, we find the following relation

$$f_+ = f_- + 2g_s\mu_B B_z\,. \tag{4.3}$$

On the other hand, if indeed (as we suspect) the main contribution to the line broadening is δB, either from local fields or an external field gradient, we can set $\delta\epsilon \simeq 0$ and obtain

$$f_+ = 2D_{\rm gs} - f_-\,. \tag{4.4}$$

In both cases f_+ selects NVs of a specific population (i.e., particular $d^{\parallel}\delta\epsilon$ or particular δB_z) inside $m_s = 0$. If we set a MW field at frequency f_+ we can think of f_+ as a pump that causes a spectral hole at f_- which can be detected by a probe with frequency f_-. Notice that while in Eq. (4.3) there is a +1 ratio between f_+ and f_-, there is a -1 ratio in Eq. (4.4). We will use this difference to our advantage by observing changes in f_- (probe) compared to changes in f_+ (pump) and deduce the main contribution to the line broadening.

NV's in an ensemble differ not only by their local strain or magnetic environment as described above, but also in the projection of the nuclear spin, m_I, of the nucleus of the N^{14}, for which I=1. In a hole burning saturation experiment we label the central transition frequencies (of a certain m_I population) by f_+^0 and f_-^0. Now, if we set the MW field to the resonance of, say, the $|m_s = 0; m_I = +1\rangle$ to $|m_s = +1; m_I = +1\rangle$ transition, , it will transfer $m_I = +1$ population to the $m_s = +1$ level with $\Delta m_I = 0$ and burn a hole in the $|m_s = 0; m_I = +1\rangle$ level for NVs that are

experiencing the same δB (or $D^{\parallel}\delta\epsilon$) field. We can describe f_+ as a pump field and f_- as a probe, and expect that if we apply a pump at f_+, we will cause a spectroscopic hole at f_-.

It was suggested in [30] that the spectroscopic hole should have a reduced linewidth compared to an ODMR experiment, as it does not suffer from inhomogeneous broadening since f_+ and f_- are addressing NVs of the same type of population (same δB or $d^{\parallel}\delta\epsilon$). Specifically, a smaller line width (up to bounds set by other origins such as the natural line width or power broadening), is expected every time measurement time (i.e. lock-in cycle time) is faster than the correlation time of paramagnetic impurities such as P1 (nitrogen) centers, NV^0, NV^-1, and so on. Standard samples contain about 1.1% of the C^{13} impurity which has the long correlation time of 10 ms. Hence, typical lock-in frequencies in the range of kHz, should remove the linewidth contributions from such a source. Regarding strain fields, we do not have very good knowledge of their correlation times, and it is probably dependent on the type of phonons which are excited in the sample. Let us note, that in our experiments we went all the way to MHz lock-in frequencies, and could not observe with this method any further reduction of the linewidth relative to what was observed in [30] where a kHz frequency was used.

Focusing on Eq. (4.4) we can see that f_- dictates the location of f_+ (and the other way around); if the central transition frequency to state $|m_s = +1; m_I = +1\rangle$ is f_+^0, and f_-^0 for state $|m_s = -1; m_I = +1\rangle$, and we only slightly change f_+ (i.e. interact with a different population) so that we stay well inside the $|m_s = +1; m_I = +1\rangle$ HF transition line, i.e., $f_+ = f_+^0 + \delta f$ with $\delta f < 1\,\mathrm{MHz}$, there should be also a corresponding change in the conjugate frequency, $f_- = f_-^0 - \delta f$ and it will in fact shift the location of the hole. It is important to shift the pump by no more than a few hundred kHz since a large shift in the pump frequency (say, 2 MHz) can cause a masking effect where the hole seems to move by 2 MHz, but we are actually addressing now different m_I populations, as the splitting between different m_I transitions is only 2.16 MHz and a typical linewidth is larger than 1 MHz..

We neglect the interaction of the nuclear spin with the magnetic field, since it is almost 2000 times weaker than the interaction with the electronic spin, and the broadening that small local magnetic fields generate, through the nuclear spin, can be ignored. Under this assumption, the HF states are not directly sensitive to magnetic fields, so the broadening that the transitions experience is due to δB (again, focusing on Eq. (4.4)) that affects the resonance frequency between the m_s Zeeman sub-levels; namely, for each local NV center there is a different transition frequency due to different local δB that shifts a little bit the m_s transition frequency compared to another NV that is experiencing different δB. As a consequence, when we measure an ensemble, we average over all the transition frequencies of the different NVs and observe a broadened line shape. Shifts in the m_s central frequency will also shift the HF resonance frequencies by the same amount, and therefore will introduce a broadening in each HF transitions as well. Thus, it is sufficient to investigate the origins of the inhomogeneous broadening of the HF transitions by just looking at the spin Hamiltonian and neglecting the nuclear spin interaction, as was done in Eq. (4.1).

4.2 Detecting the Hole

In order to now establish which model is correct, Eq. (4.3) or Eq. (4.4), we want to monitor changes in the hole frequency with reduced FWHM compared to ODMR, and more importantly to monitor changes in hole location as a result of different pump MW frequencies, according to Eq. (4.3) or Eq. (4.4). To this end, we use an amplitude modulated MW pump field with a fixed frequency that corresponds to a specific HF transition (f_+^0), and scan around f_-^0 with a CW probe field. We set the scan wide enough to go over all three HF transitions. During the scan we measure the modulated fluorescence coming out of the diamond as a function of the probe frequency using a lock-in amplifier (Fig. 2.1). When the pump beam is exactly on resonance (f_+^0) but the probe beam is far from resonance, the probe will not affect the lock-in signal and we will get a high contrast in

the lock-in due to the modulated pump beam. As we bring the probe beam closer to resonance, the probe beam and the pump beam are now addressing NVs of the same population (same m_I and δB or $\delta\epsilon$) and since the probe is CW there is less modulated fluorescence light and we get a reduction in the lock-in signal. Notice that we borrow the terms 'probe' and 'pump' from vapor experiments where one measures changes in probe intensity, but here we neither measure probe nor pump but actually measure the modulated fluorescence that is associated with the pump field, not probe. The total result of this fixed-pump scanned-probe process is the creation of a spectroscopic hole at f_-^0.

In the derivation of Eq. (4.4) we assumed that the local magnetic field is constant. This might be true for local fields that originate in the gradient of the external field, but as noted above, in the case of a local field generated by nitrogen impurities (often referred as P1) or due to the ^{13}C spin bath, this assumption is limited by the correlation time of the field which is $\sim 10\,\text{ms}$ for the ^{13}C [31] and $\sim 10\,\mu\text{s}$ for P1 [32]. We repeated the saturation spectroscopy experiment three times. In each experiment, the pump was set to the transition frequency (f_+^0) of a different HF state and the results, as presented in Fig. 4.1, show a clear reduction in the spectroscopic linewidth that could be

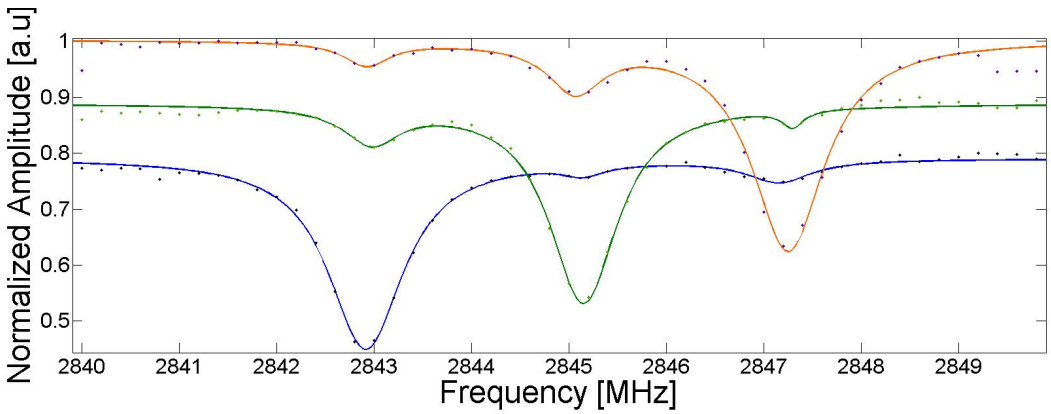

Figure 4.1: Spectroscopic holes using the fast setup (lock-in frequency of 36.6 kHz). Data in dots, fit in solid line. The color code is the same as in Figs. 1.3 and 3.5; in red line the pump is set to the $m_I = +1$ central transition frequency. In green and blue lines the pump is set to the $m_I = 0$ and $m_I = -1$ transitions respectively. In each hole we can clearly see the other two transitions as small side dips. A discussion regarding the possible origins of the side dips can be found in App. B. The average linewidth of the hole is 0.9 MHz which is $\sim 200\,\text{kHz}$ less than an ODMR width.

attributed to the removal of inhomogeneous broadening. The amount of width reduction can vary between samples, as different diamonds have different environments, and even the same sample can have different results between two setups as there could be changes in the external field gradient or the impurities generating the inhomogeneity broadening may not be distributed isotropically. In addition, there could be a difference in MW power between pump and probe that can affect the linewidth through power broadening. Therefore, it is hard to tell what is the remaining dominant source of the linewidth. Similar results were achieved in [30] for a similar HPHT diamond.

The next step in validating Eq. (4.4) is to show that we can shift the hole by $-\delta f$ if we shift the pump to $f_+^0 + \delta f$. To this end, we made a series of tests where we changed the pump frequency with a 100 kHz step size, starting at the central frequency of the $m_I = 0$ transition, and scanned with the probe to observe the hole. Each test yielded a hole that was later fitted to a Lorentzian and the hole location was extracted. We plotted the hole location vs. the pump frequency and made a linear fit to extract the slope. In the fast setup we find a slope of -0.59 and in the slow setup we find -0.99 with the same magnet as in the fast setup. In the slow setup and with the different magnet we find -0.83. In all experiments we expected a slope of -1 regardless of the different magnet or setup. We believe that one possible reason for the inconsistency in the slope value, could be thermal fluctuations: if we look again at Eq (4.4) we can see that not only can f_+ generate a

change in f_- but so can $D_{\rm gs}$. $D_{\rm gs}$ is not constant and can have thermal fluctuations as high as $-75\,$kHz/K at room temperature [33]. Thus, even a small temperature changes such as $0.5\,$K can appear as a $75\,$kHz change in hole location.

At this point, although we did show a negative correlation between f_+ and f_-, it seems that we did not prove strongly enough that the main inhomogeneous broadening mechanism is due to the local magnetic field environment. Similar uncertainties were observed in the work done in [30] as was communicated to us in private communications. To improve this situation, we came up with a new method to validate Eq. (4.4), and this is the topic of the next chapter..

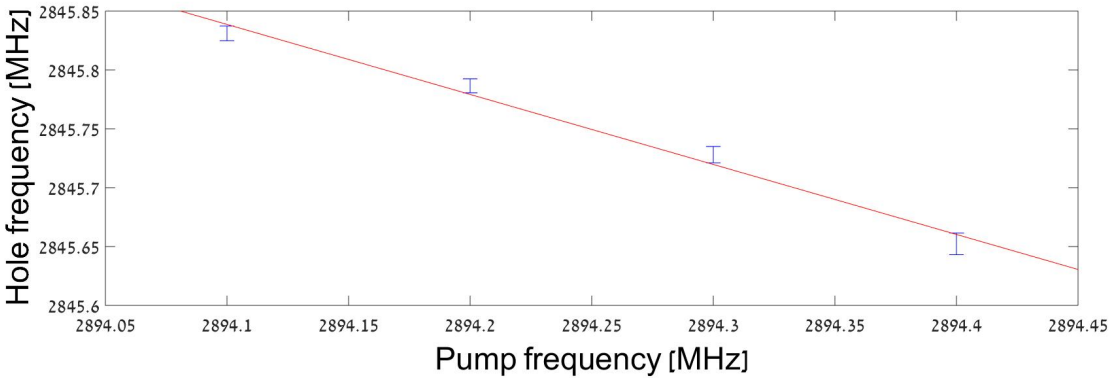

Figure 4.2: Migration of hole (f_-) using the fast setup ($36.6\,$kHz). Blue data, red linear fit. The pump frequency was changed in small steps of $100\,$kHz. The fit returns a slope of -0.59 ± 0.21 and $4567 \pm 615\,$MHz for the constant (which according to Eq. (4.4) is expected to be $2D_{\rm gs} = 5740\,$MHz).

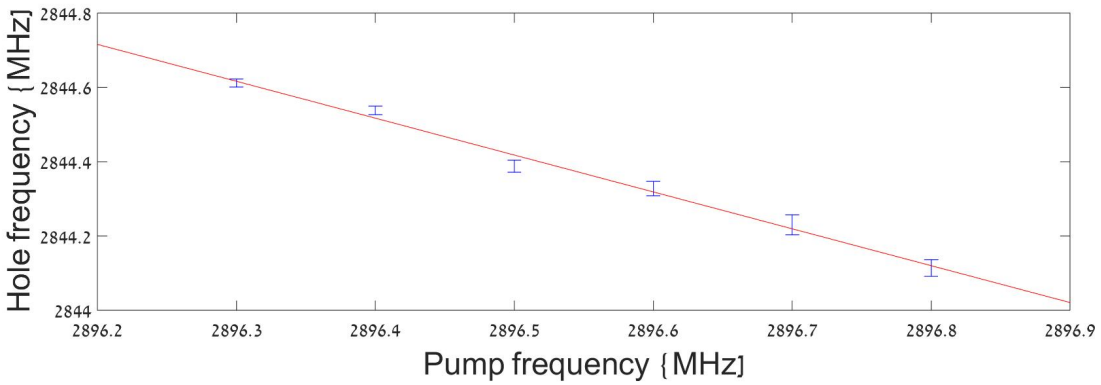

Figure 4.3: Migration of the hole (f_-) using the slow setup ($426\,$Hz) with the same magnet as in the fast setup. Blue data, red linear fit. The pump frequency was changed in small steps of $100\,$kHz. The fit returns a slope of -0.99 ± 0.13 and $5809 \pm 396\,$MHz for the constant (which according to Eq. (4.4) is expected to be $2D_{\rm gs} = 5740\,$MHz). The slight change in the pump frequencies relative to Fig. 4.2, is probably due to a re-alignment of the setup together with a strong gradient of the external magnetic field.

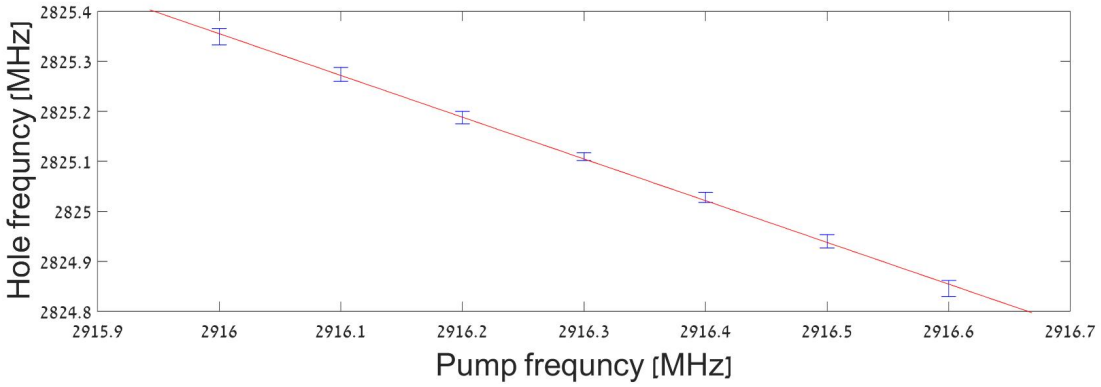

Figure 4.4: Migration of the hole (f_-) using the slow setup (426 Hz) . In this version of the slow setup we used a different magnet, as can be seen in the different magnetic resonance frequency. Blue data, red linear fit. The pump frequency was changed in small steps of 100 kHz. The fit returns a slope of -0.83 ± 0.03 and 5259 ± 87 MHz for the constant (which according to Eq. (4.4) is expected to be $2D_{\mathrm{gs}} = 5740$ MHz).

Chapter 5

"Doppler-Free" Spectroscopy

In the previous chapter we tried to provide proof that Eq. (4.4) was at work, thus proving that varying local magnetic environments are the cause of the observed inhomogeneous broadening. Although our results were in qualitative agreement with Eq. (4.4), the quantitative agreement was far from satisfactory. In order to test the model more accurately, with our existing equipment, we devised a different method to validate the above equation using a novel type of NV spectroscopy. In addition, the new spectroscopy exhibits a FWHM linewidth that is half of the saturation hole width, and thus the new method may prove advantageous for sensing applications.

5.1 Theory

Our new spectroscopic method is analogous to Doppler-free spectroscopy in vapor: in Doppler-free spectroscopy we use two counter-propagating laser beams with the same frequency and observe the interaction of the laser light with atoms having different velocities. The atoms can be classified according to their velocities, where $P(v)$ is their velocity probability distribution. Due to the Doppler effect, one laser beam will interact with atoms of class $P(v)$ while the other interacts with $P(-v)$. Therefore, the two fields will always interact with different populations (due to the Doppler shift) except for the population with zero velocity (with respect to the optical axis). In such a case, the Doppler shift is zero and if the radiation field is resonant with the atomic transition, both fields will address the same population. If the pump field has higher amplitude than the probe, then it will "burn a hole" in the ground level of the $P(v = 0)$ population, which can be detected by the probe as the pumped atoms will barely interact with the probe and we expect to observe a reduction in probe absorption (or increased probe intensity). Since the width of this hole is only limited by the atomic natural linewidth and the laser linewidth, the observed linewidth is much narrower than the Doppler broadened linewidth.

Our method is analogous to Doppler-free spectroscopy in vapor in the sense that in both cases we use two radiation fields that always address different populations except when both fields are at resonance with the center of the broadened distribution. While in the vapor experiment the different populations have different velocities, here the broadening mechanism (as we suspect) is due to the fact that each of the NVs in our ensemble can have a slightly different magnetic environment, $\delta\mathbf{B}$, and consequently a different transition frequency causing inhomogeneous broadening. We replace the counter propagating beams in the vapor experiment with f_+ (pump) and f_- (probe) and instead of fixing the frequencies of the radiation fields to be the same and scan for different frequencies- as in Doppler-free spectroscopy, we rather fix the frequency gap between the two fields and then scan at different pump-probe frequencies while keeping the frequency gap constant. Focusing on the $m_I = 0$ transition, we fix the frequency gap to be $\Delta f = f_{m_s=+1;m_I=0} - f_{m_s=-1;m_I=0}$, where the latter are the resonance frequencies, and we scan with a CW probe while the lock-in modulated pump follows.

When the probe is on the $m_I = \pm 1$ transition the pump is on the $m_I = \mp 1$ transition and the probe has no impact as it always addresses m_I states that are different than those addressed by the modulated pump, and we expect to see a regular ODMR signal generated by the pump. When we scan within the $m_I = 0$ linewidth, both radiation fields address the same m_I. However, when they are not directly on resonance, the negative sign in Eq. (4.4) dictates that they are still addressing different populations; when the probe and pump fields are "red-detuned" with respect to the transition frequency, the hole is "blue-detuned" and the probe is not at the hole frequency and has no impact on the lock-in signal. Only when both fields are at resonance (f_-^0 and f_+^0) will they address the same population and we should observe a narrow "Doppler-free" type hole at the center of the ODMR peak.

We modeled our expected experimental line shape as the sum of four Lorentzians. We started by assuming that the HF transitions have the same amplitude and derived the general form:

$$S(f_+) = \sum_{i=-1}^{+1} a_1 \frac{\gamma_1}{2} \frac{1}{(f_+ - f_{+_i}^0)^2 + (\frac{\gamma_1}{2})^2}\,, \tag{5.1}$$

where f_+ is the pump frequency (+ represents transition to $m_s = +1$), $f_{+_i}^0$ is the transition frequency to $m_s = +1$ with $m_I = i$ and a_1 and γ_1 are the amplitude and FWHM respectively. Thus, Eq. (5.1) simply describes a regular ODMR signal of the HF transitions using lock-in (i.e., three Lorentzians with equal positive amplitude and width). As explained above, the CW probe affects the pump lock-in signal only when both fields are near $m_I = 0$. Thus, the hole in the pump signal should be described by a single Lorentzian. The problem is that the hole location is not constant but rather governed by the pump location (remember Eq. (4.4)). Therefore, the general form of the hole can be described using the following Lorentzian:

$$h(f_-, t) = a_2 \frac{\gamma_2}{2} \frac{1}{(f_- - t)^2 + (\frac{\gamma_2}{2})^2}\,, \tag{5.2}$$

where f_- is the probe frequency ($-$ represents transition to $m_s = -1$. Remember that f_- is at a fixed distance of Δf from the pump), $f_{-_i}^0$ is the transition frequency to $m_s = -1$ with $m_I = i$ and a_2 and γ_2 are the amplitude (with a negative sign as this is the hole) and FWHM respectively. The location of the center of the Lorentzian, t changes with f_+ as Eq. (4.4) states. Due to the fixed frequency gap, Δf, between the pump and the probe, we have a situation in which for example if f_+ (pump) is 1 MHz below $f_{+_i}^0$, then f_- (probe) is 1 MHz below $f_{-_i}^0$, but t (hole) will be 1 MHz above $f_{-_i}^0$ according to Eq. (4.4), and if f_+ is 2 MHz below $f_{+_i}^0$, then f_- is 2 MHz below $f_{-_i}^0$ but t will be 2 MHz above $f_{-_i}^0$ and so on. Thus, taking δf to be the frequency difference (i.e., detuning) between the hole location and resonance, the combination of Eq. (4.4) and Δf yields:

$$f_{-_i}^0 = \frac{t + f_-}{2}\,, \tag{5.3}$$

which allows us to express t as a function of f_-. We can now present $h(f_-, t)$ as $h(f_-)$, but since S is dependent on the pump frequency, f_+, it will be more natural to write h as $h(f_+)$ rather than $h(f_-)$. We therefore use $f_+ = f_- + \Delta f$ and find (taking $m_I = 0$ as Eq. (5.3) is valid for all m_I):

$$f_- - t = 2f_- - 2f_{-_0}^0 = 2(f_+ - \Delta f) - 2(f_{+_0}^0 - \Delta f) = 2f_+ - 2f_{+_0}^0\,. \tag{5.4}$$

We now plug it into Eq. (5.2) to get

$$h(f_+) = a_2 \frac{\gamma_2}{2} \frac{1}{(2f_+ - 2f_{+_0}^0)^2 + (\frac{\gamma_2}{2})^2}\,, \tag{5.5}$$

and we can rearrange it to get a final result:

$$h(f_+) = a_3 \frac{\gamma_3}{2} \frac{1}{(f_+ - f_{+_0}^0)^2 + (\frac{\gamma_3}{2})^2}\,, \tag{5.6}$$

where $a_3 = 0.5a_2$ and $\gamma_3 = 0.5\gamma_2$. $h(f_+)$ is a Lorentzian that depends only on f_+ just as the ODMR Lorentzians, $S(f_+)$, and has half the amplitude and half the width of the hole. The total outcome signal of this experiment is the sum of $h(f_+)$ and $S(f_+)$. We plugged experimental values into the above model and made a phenomenological simulation of the four Lorentzians (Fig. 5.1a) in order to describe the behavior of the new spectroscopic signal. The simulation predicts that in the current settings we should observe a small hole at the center of the $m_I = 0$ transition with half the width of the hole, and that the other two m_I transitions ($m_I = \pm 1$) will not be affected.

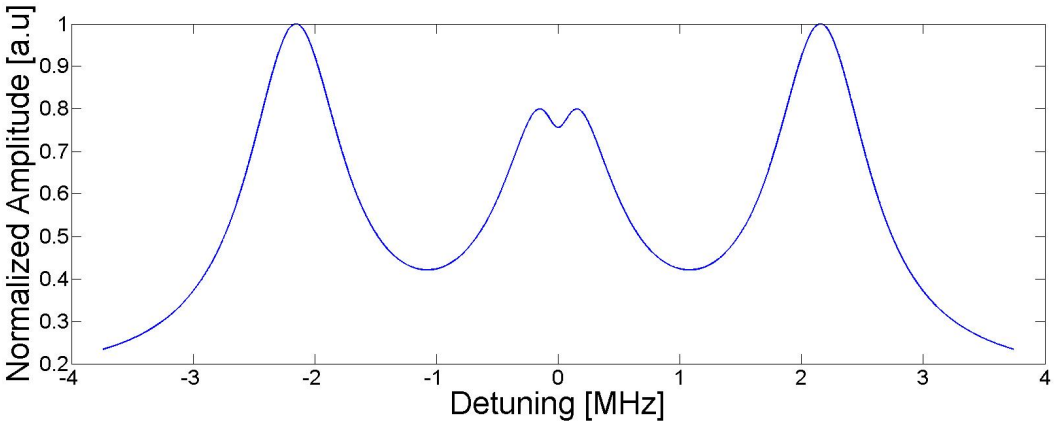

(a) Phenomenological simulation of "Doppler-free" type spectroscopy. We plotted the three Lorentzains of the ODMR (Eq. (5.1)) together with Eq. (5.6). The parametrs were taken from the results of ODMR and hole experiments with fast setup (36.6 kHz lock-in modulation. See Ch. 2). The x axis represents the detuning of the f_+ (pump) from $f^0_{+_0}$ (i.e., δf). The small hole at center is due to the fact that only when both fields are addressing the same population the probe can "steal" population from the pump. The two Lorentzians at the sides are the ODMR line shape generated by the probe-pump interplay.

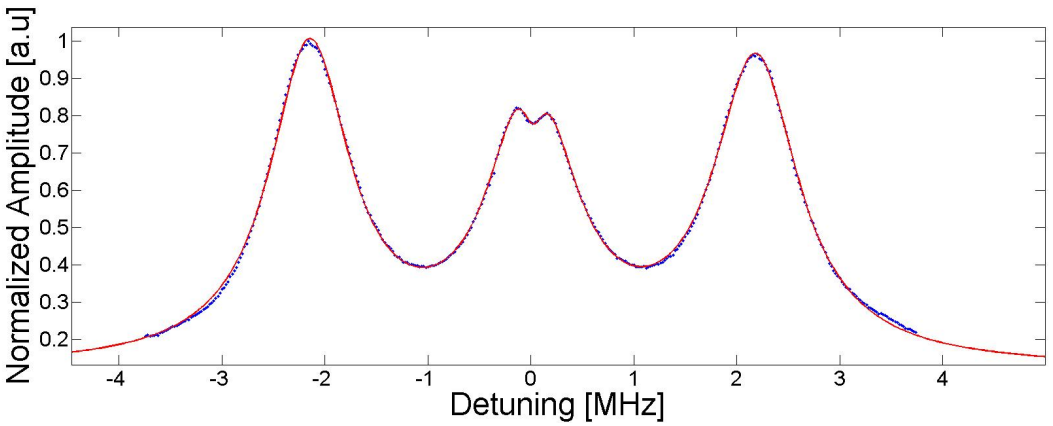

(b) Experimental results for "Doppler-free" type spectroscopy using the fast setup (36.6 kHz lock-in modulation). The data is shown in blue and the red is a fit to four Lorentzians. The x axis represents detuning of the f_+ (pump) from $f^0_{+_0}$ (i.e., δf) as measured in an ODMR experiment. The width of the hole is 338 ± 53 kHz, compared to a 850 ± 52 MHz hole width as seen in Fig. 4.1. The center of the two Lorentzians of interest coincides with a small 6 ± 8 kHz difference and the data has an excellent fit to the model with 0.999 R square value. This implies that the hole indeed follows the pump with a -1 ratio, or else they would not coincide or the line shape would be deformed thus reducing the goodness of the fit.

Figure 5.1

5.2 Experimental Results

In order to confirm the simulation and as a consequence to establish that the main contribution to the inhomogeniuos broadening is local magnetic fields, we conducted the following experiment: using the results of an ODMR experiment we calculated the frequency gap, Δf, between the transition from $|m_s = 0; m_I = 0\rangle$ to $|m_s = +1; m_I = 0\rangle$ and from $|m_s = 0; m_I = 0\rangle$ to $|m_s = -1; m_I = 0\rangle$. We fixed the frequency gap between the CW probe and the modulated pump to be Δf and made a scan around the transition to the $m_s = +1$ level with the pump (while the probe follows). We used the fast setup (36.6 kHz lock-in modulation) and all the experimental parameters are the same as in the ODMR and hole experiments, except that a lower step size was chosen. The experimental results (Fig. 5.1b) show two positive Lorentzians at the location of the transition frequencies to $m_I = \pm 1$ and at the transition to $m_I = 0$ we observed a positive Lorentzian with a Lorentzian-hole at its center. The results are in good agreement with the phenomenological simulation (Fig. 5.1a). The measured Doppler-hole at the center of the $m_I = 0$ transition has a width 0.397 ± 0.067 times lower than the width of the saturation spectroscopy hole, as measured in Fig. 4.1 (theoretically, as noted above, we would expected the factor to be 0.5). The location of the hole, as extracted from the fit is 0.019 ± 0.005 MHz away from the location of the $m_I = 0$ transition as measured in an ODMR experiment, while the location of the $m_I = 0$ transition is 0.013 ± 0.003 MHz away from the location of the $m_I = 0$ transition as measured in an ODMR experiment. The centers of the two Lorentzians are therefore shifted one from the other by only 6 ± 8 kHz, in good agreement with the theoretical model. The goodness of the fit to our model of four Lorentzians, represented by the R-square value, is 0.999.

Combined with the results obtained using narrow saturation spectroscopy, the "Doppler-free" spectroscopy clearly shows that the local magnetic fields are the main cause of the inhomogeneous broadening. Furthermore, we have shown that our new spectroscopic method can reduce the hole width compared to saturation spectroscopy by half and may thus provide increased sensitivity in magnetic sensing.

Chapter 6

Summary and Conclusion

In Ch. 3 we described the importance of the linewidth and that a deeper understanding of the origins of the inhomogeneous broadening in an ensemble could prove useful in a variety of fundamental studies and applications.

A simple derivation of the Hamiltonian showed that hole burning saturation spectroscopy can shed more light on the origins of the inhomogeneous broadening, by monitoring the response of the spectroscopic hole to a change in the pump frequency. To this end, we used a pump MW field to excite NVs into the $m_s = +1$ state thus burning a spectroscopic hole in the ground state in the process. A second CW MW field enabled us to probe that hole by scanning around the $m_s = -1$ transition frequency. Once both fields address the same population (same nuclear spin projection and same local magnetic environment) in the ground state, a reduced-width spectroscopic hole (compared to an ODMR scan) should appear. Using our experimental setup we were able to observe a reduced-width hole with similar results to those obtained in [30].

Under the assumption that the origins of the inhomogeneous broadening are local magnetic fields, we can shift the pump frequency in the hole burning spectroscopy and expect a corresponding shift in the hole location with a negative sign. When we tried to validate this hypothesis, i.e. observe a corresponding change in the hole location due to a change in the pump location, we had an error as large as 40% compared to theory. This led us to come up with a new method that could show that the hole moves with the pump in a pump-hole ratio of -1. To this end, we introduced a novel spectroscopy that combines elements from the Doppler-free spectroscopy done in vapor.

In the "Doppler-free" type spectroscopy we fixed the frequency gap between the pump and probe to be $\Delta f = f_{m_s=+1;m_I=0} - f_{m_s=-1;m_I=0}$ where f is the resonance transition. We then scanned around the $m_I = 0$ transition frequency (and $m_s = -1$ for probe and $m_s = +1$ for pump). We observed a Doppler hole inside the transition line shape with half the width of the hole in the saturation spectroscopy, that coincided with the ODMR line shape of the $m_I = 0$ transition, in good agreement to theory. Thus, we confirmed with high likelihood that the main contribution to the inhomogeneous broadening comes from local magnetic fields.

Appendix A

Optical switch

Acousto-optics modulators(AOMs) are devices used in many optical systems to control laser intensity, frequency and direction of propagation. An RF driver (80 MHz for our AOM) generates vibrations using a piezoelectric transducer that generates moving acoustic waves in a crystal to which it is attached. Once the laser hits the crystal, it sees repetitive moving wave fronts (although some AOMs work with standing waves), or in other words, a grid. The acoustic waves changes the local pressure inside the crystal and as a consequence change the refractive index. Using subscripts i and d to denote the initial and deflected light waves respectively, and the subscript s to denote the sound wave, vector analysis (i.e., conservation of momentum) of the wavenumbers $\mathbf{k}_i = k_s + k_d$ yields

$$2\lambda_s \sin(\theta) = \frac{\lambda_i}{n}\,, \tag{A.1}$$

where θ is the deflection angle, n is an integer diffraction order, and $\lambda = \hbar k$. Here we have assumed that $k_s \ll k_i$, so $k_i \simeq k_d$. This condition is identical to the first Bragg condition employed in X-ray crystallography, where the periodic wavefronts are analogous to the atomic planes separated by a constant gap in Bragg diffraction. Here however [34], the wavefronts are moving, causing shifts of ω_s in the light frequency, which can be interpreted as a Doppler effect in the Bragg scenario. In addition, this derivation does not include high orders of diffraction unlike the Bragg diffraction, although in reality we do get higher orders in an AOM, due to the sinusoidal modulation and finite thickness if the acoustic waves [34].

If we position an iris in the path of the 1st-order order diffraction pattern, the light can pass through only if the AOM is turned on, but when the AOM is off, the laser will be blocked by the iris and will not continue to the optical setup. using such an iris and modulating of the AOM (on-off), we can effectively modulate the laser on-off at a nano-second rate. This experimental ability is necessary in many experiments, such as: measuring Rabi oscillations, Ramsey fringes, etc.

Let us assume that we polarize the laser parallel to the optical table before it enters the AOM, and add a quarter-wave plate (QWP) between the AOM and the mirror. In such a setup the laser beam will go through the QWP twice, which effectively serves now as a half-wave plate, so that the laser will emerge from the double pass AOM with its polarization perpendicular to the table. inserting a polarizing bean splitter (PBS) before of the AOM enables us to separate the incident and reflected laser beams (which overlap spatially) and we can continue to build our optical setup in the path of the outgoing beam.

Appendix B

Side Dips

In Fig 4.1 we saw that along with the main hole in the saturation spectroscopy, there are additional two side dips that are associated with the other two nuclear resonances. Since the theory did not anticipate this result, and it was hardly noticeable in the results of [30], we started to search for a technical explanation, under the assumption that this is an experimental artifact.

When the probe frequency is on resonance with a nuclear spin transition that has a different m_I number than the one the pump is addressing, it excites the population to $m_s = -1$ which causes a reduction in the total amount of fluorescence although the amount of population that the pump is modulating is left unaffected. Therefore, the total result is a DC shift in the fluorescence. Since the fast lock-in has a 20 kHz high pass filter a DC change should not affect the lock-in signal. We can look more deeply into this process and realize that the probe is not just simply moving the population into the excited state, but actually causes Rabi oscillations. We estimate the oscillations (upon previous tests that are not presented in this thesis) to have a time period of no more than a few micro-seconds, which could be potentially very close to the 36.6 kHz frequency that we are using. But if indeed this is the case, then the total signal should increase when the probe hits resonance, whereas we are getting a reduction in contrast. Furthermore, the side dips phenomenon was observed also in the slow lock-in as can be seen in Fig. B.1, where frequencies of dozens of kHz such as Rabi cycles are filtered. To conclude, it is not an artifact related to the lock-in amplifier.

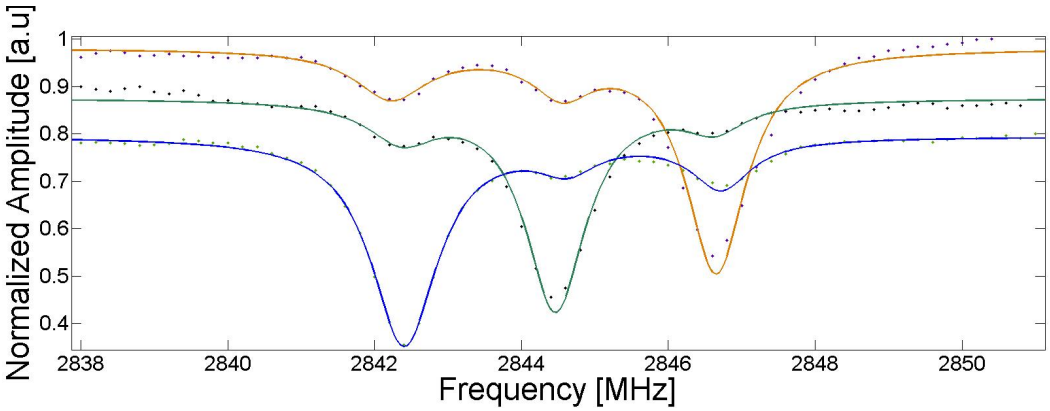

Figure B.1: Saturation spectroscopy in the slow setup. The color code is the same as in Fig. 4.1. There are clear side dips for each m_I population which were also seen in the fast setup. Thus, the side dips are not related to a DC shift that the probe could have made (as a DC signal is filtered by the fast lock-on) nor it is related to possible oscillations of the fluorescence due to Rabi oscillations (as fast signals are filtered by the slow lock-in).

Another possible solution that we thought could explain the side dips is the fact that both pump

and probe are combined using a beam combiner, and the total signal is then connected to a 16 W amplifier. It could be that when both MWs are on, each frequency is amplified by 8 W and when the pump is off the probe is getting all the 16W and the probe is also being modulated de facto at the reference frequency. This can also explain the fact that we see the dips in the slow setup as well. In order to confirm this hypothesis, we used two separate MW amplifiers and antennas, and connected the pump and probe to each one. We calibrated the post-amplifier pump and probe signals to have roughly the same amplitudes and again made saturation spectroscopy where a modulated pump at 36.6 kHz was set at a fixed frequency and scanned with a CW probe. The results, presented in Fig. B.2 still show side dips and eliminate the possible new explanation of side dips due to a combined electronic circuit.

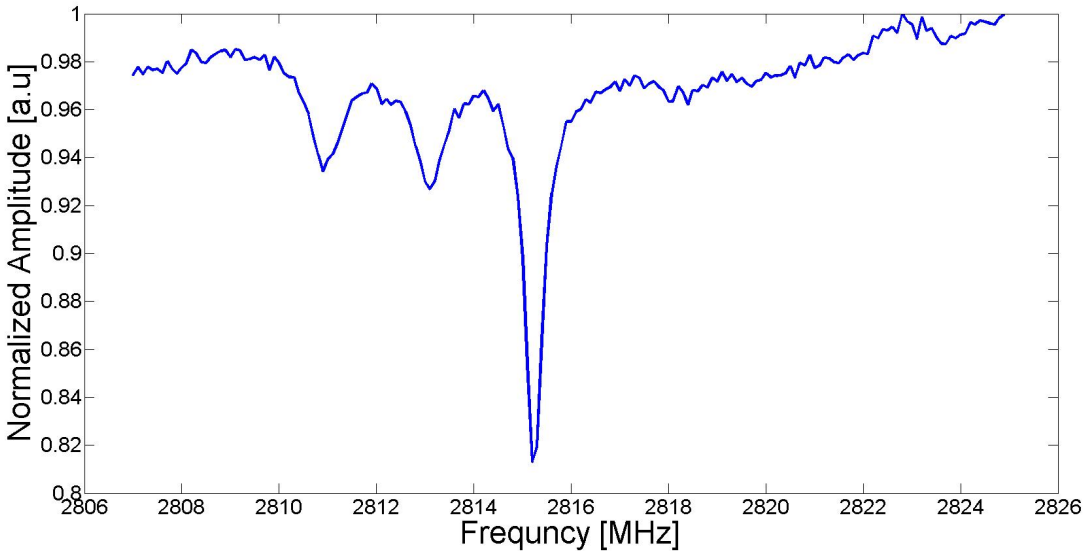

Figure B.2: Saturation spectroscopy using 2 electronic circuits and fast lock-in amplifier. Even though we use two separate amplifiers and two separate antennas, we still observe side dips, which implies that the cause for this effect cannot be attributed to the use of a single antenna and a single amplifier for both MW fields.

A third possible artifact that we checked was the existence of side bands on the frequency of the pump field. Since we multiply the pump MW signal (a sine wave) with a square wave (the modulation), then according to Fourier theory we should get more frequencies in addition to the carrier (the pump). In order to verify this possibility, we positioned a loop antenna next to the MW antenna, and connected the loop antenna to a spectrum analyzer (Rohde Schwarz FSP13) in order to detect the EM waves that the MW antenna sends. In addition we also connected the spectrum analyzer to the MW generator clock. When we turned the modulation off, we observed a very sharp, single MW frequency as can be seen in Fig. B.3. But when we turned the modulation on at 36.6 kHz the spectrum analyzer showed many side bands (Fig. B.4). Each side band has the same AM modulation as the carrier (Fig. B.5). Therefore, a side band that is at ~ 2.16 MHz away from the carrier (2.16 MHz is the frequency separation between two nuclear energy levels) could cause a modulated fluorescence that will be detected by the lock-in amplifier. Therefore, when we set the carrier to be at the transition frequency of, say, $m_I = +1$ and multiply it with a square wave, then also the $m_I = 0$ population will feel a modulated MW field at resonance, thus increasing the lock-in signal, and once the probe CW MW will be on resonance with $m_I = 0$ then it will reduce the amount of modulated fluorescence and consequently the lock-in signal even though the probe is not at the same m_I population transition frequency as the pump. To fully confirm this, we shifted the carrier

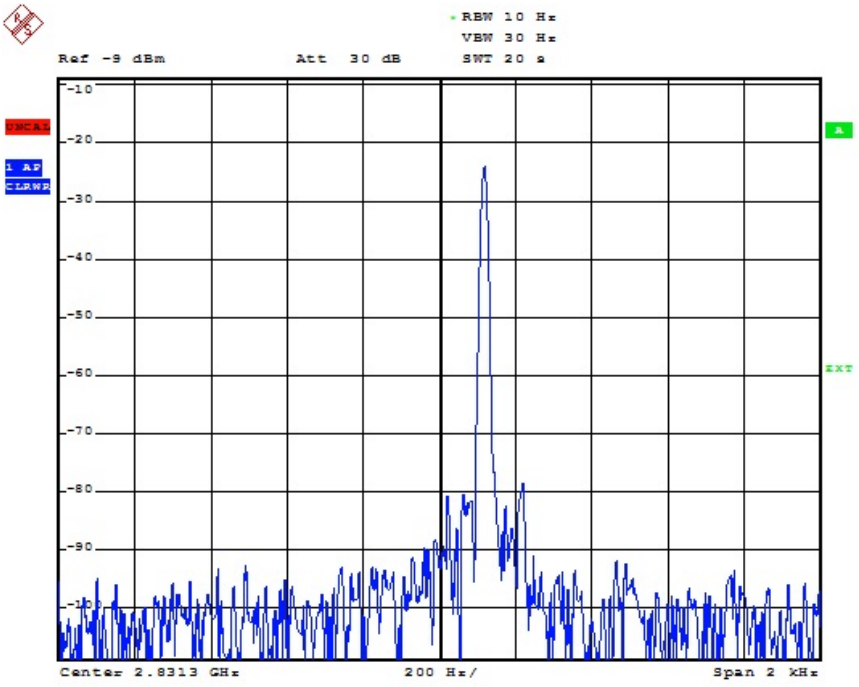

Figure B.3: MW signal without modulation. We set the pump frequency to be 2831.3 MHz at CW operation mode and turn the MW switch off (modulation off). The spectrum analyzer shows that the MW signal has a very sharp width (only a few Hz width).

frequency by 2.16 MHz from 2831.3 MHz which is the resonance of $m_I = +1$ to 2829.14 MHz which is off resonance (i.e., we did not shift it towards $m_I = 0$). So if we are completely off resonance and still observe spectroscopic dips, we could assign it to the side bands. The results, as depicted in Fig. B.6 clearly support the explanation that the side bands are responsible for the side dips effect.

However, more work needs to be done to fully close this issue. For example, as can be seen in Fig. B.4, the side bands 2.16 MHz away from the carrier are some $30 - 40$ dB weaker than the carrier. The question then arises as to why the side dips in Figs. B.1 and B.2 are as strong as they are, up to a factor of 1/5 of the main lock-in dip. Furthermore, As can again be estimated from Fig. B.4, the difference in power of the side band 2.16 MHz away from the carrier and the one 4.32 MHz away, is also considerable, while in Figs. B.1 and B.2 they are quite similar in amplitude.

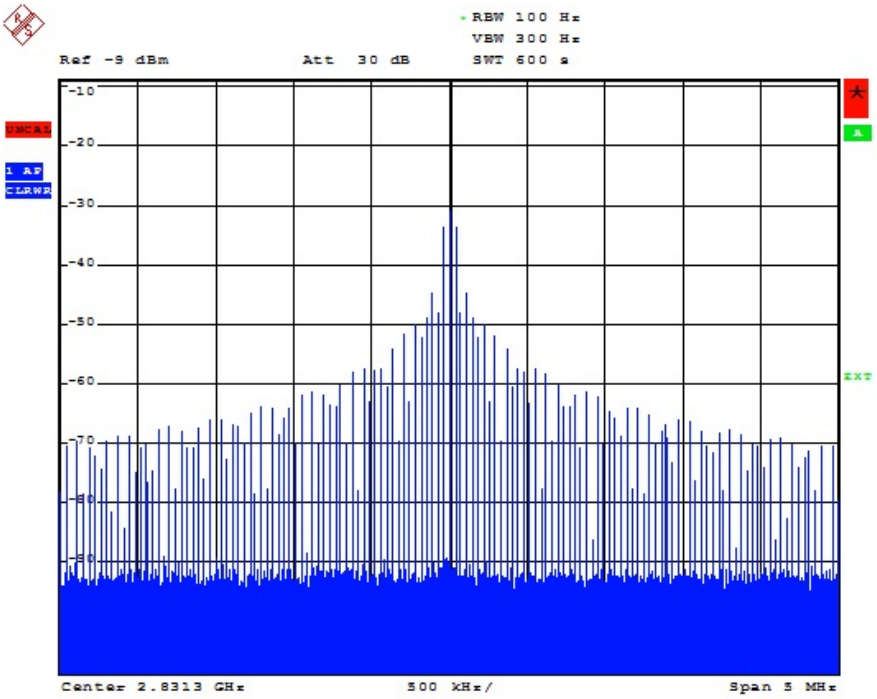

Figure B.4: MW signal with 36.6 kHz modulation. We set the pump frequency to be 2831.3 MHz at CW operation mode and turned the MW switch on-off at 36.6 kHz.

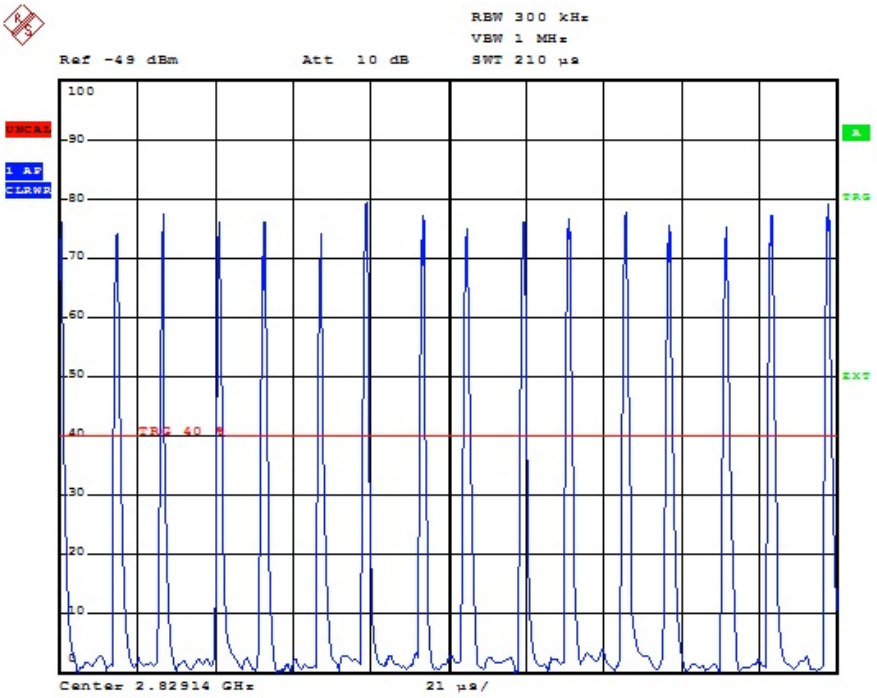

Figure B.5: Side band amplitude modulation. We set the pump frequency to be 2831.3 MHz at CW operation mode and turned the MW switch on-off at 36.6 kHz. We used the spectrum analyzer as a scope ("zero span") and observed the amplitude of 2829.14 MHz. This is about 2.16 MHz away from the pump frequency and corresponds to the frequency hyperfine splitting between the different resonances.

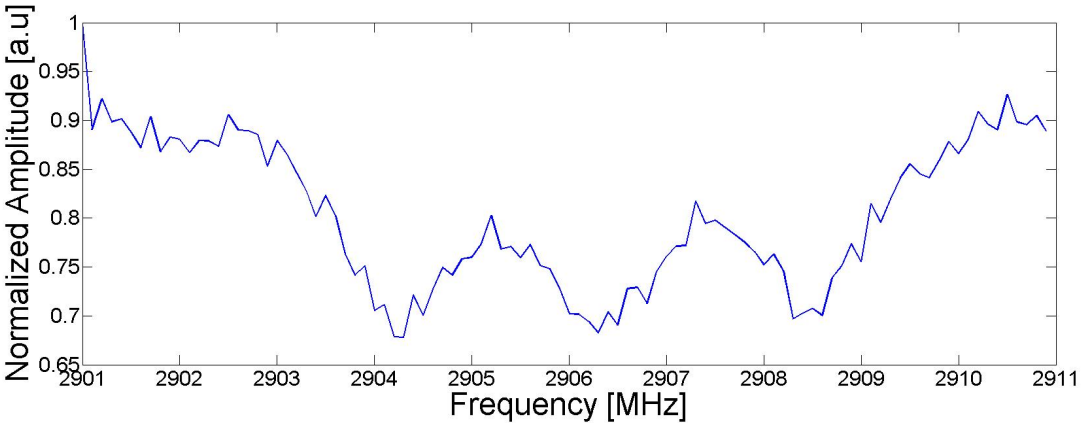

Figure B.6: Spectroscopic holes with pump off resonance. We shifted the pump frequency by 2.16 MHz away from the transition frequency of $m_I = +1$ so we are completely off resonance (i.e., it was not shifted towards $m_I = 0$, but rather in the opposite direction). Despite that the pump was off resonance there are still very noticeable side dips. This clearly confirms our suspicion that the side bands that are few MHz away from the carrier still have enough amplitude to generate oscillations that can be detected by the lock-in.

Appendix C

Outlook

In addition to the "Doppler-free" type spectroscopy experiment, we worked in parallel on another experiment which we call "the adiabaticity experiment". Here we apply a B_z magnetic field and prepare our system using green light and a MW π pulse for some Zeeman state, say $m_s = +1$. Once the system is prepared in state $m_s = +1$, we examine at the following question: what will happen to the eigenstate population if we generate a rotation of π radians of the magnetic field along the z axis from $+B_z$ to $-B_z$. If the process is adiabatic, we will move from $m_s = +1$ to $m_s = -1$ in the lab frame; in the frame of the magnetic field the system will remain at $m_s = +1$. We would stay in our eigenstate only if our rotation is slow and the amplitude is weak enough (we could also consider a rotation in the $y - z$ plane, but this case is more complicated and will not be discussed here). In order to know what exactly is "slow" and "weak", and to know the validity range of our adiabaticity, we solved the Schrödinger equation for different frequencies and amplitudes of the rotating magnetic field, and made a 3D plot (Fig. C.1) of the adiabaticity as a function of these two parameters.

In order to generate and control the magnetic fields we fabricated a chip with two crossing wires in the same plane (Figs. C.2 and C.3). By placing a [1 1 0] diamond above crossed-wire junction, the $y - z$ plane of two NV orientations will be parallel to the plane of the wires and therefore to the plane that the magnetic fields span (above the crossing junction). This enable us to rotate the effective field along the plane of the diamond by simply changing the current.

We define adiabaticity as the probability of remaining in the initial eigenstate after a π rotation, and we ignore the dynamics of the process (although our simulation shows, not presented here, very interesting dynamic during the process that we can investigate using our setup in order to shed light on the fundamental physics of two levels inter-system crossing). In addition to the fundamental physics aspect of these adiabaticity studies, this setup could also have very useful applications: for each rotation there could be a small probability for inter-system crossing (ISC) to the other eigenstate. If we repeat the rotations many times, the ISC phase can accumulate due to the Landau-Zener-Stückelberg (LZS) process and resolved as Rabi oscillations that have much longer coherence time [35] but instead of generating LZS using changing MW fields as in [35], we use oscillating magnetic fields and the Rabi oscillations are between the $m_s = \pm 1$ levels, not between $m_s = 0$ and one of the $m_s = \pm 1$ levels. An increase in the coherence time can improve the magnetic sensitivity as was shown in Ch. 3. In addition, the amplitude if the Rabi oscillations in this process is highly sensitive to the parameters of LZS tunneling (e.g., the frequency of the oscillating magnetic field) and might also prove useful in precision measurements.

Another potentially interesting experiment is to utilize the adiabaticity process to generate a superposition of the $m_s = \pm 1$ Zeeman states without the need for a MW two-photon process. We can do so by preparing the system in a Zeeman state, say, $m_s = +1$, and reducing the amplitude of the magnetic field to zero. When we do so, the system will stay in its eigenstate, but at zero magnetic field the eigenstates are not the Zeeman states but, using $|S, m_s\rangle$ notation, the eigenstates

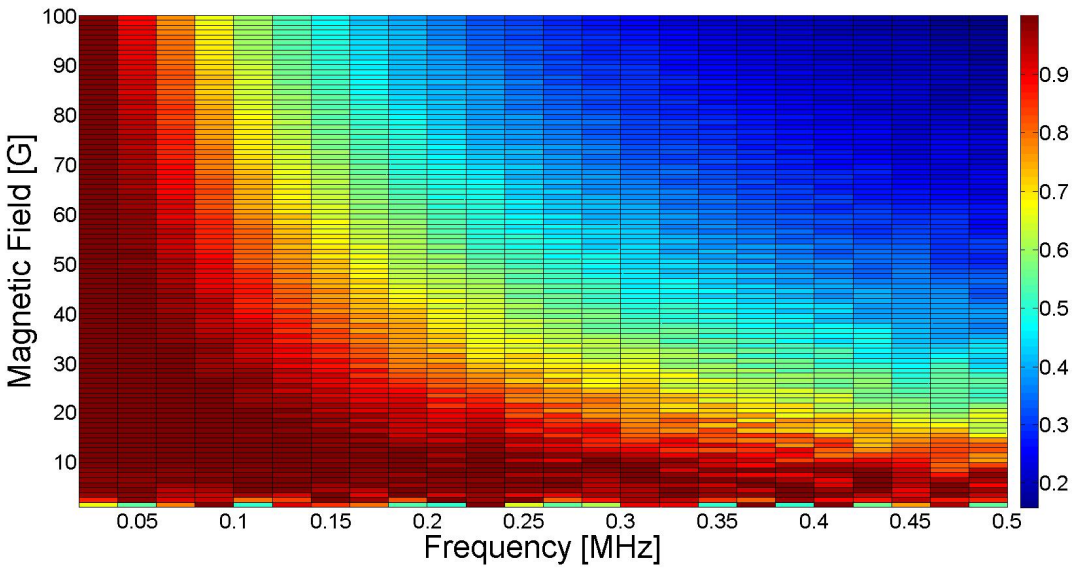

Figure C.1: Simulation of probability to stay in the initial eigenstate ($m_s = +1$) under a time dependent magnetic field of the form: $B_z(A, f) = A\cos(2\pi f t)\hat{z}$ at $t = \frac{1}{2f}$ as a function of the magnetic field amplitude (A) and frequency (f). Red is probability to stay in the initial eigenstate. It is clear that low amplitude and low frequency generate an adiabatic process. Our nano-fabricated chip can generate magnetic fields of a couple hundred Gauss and the current source can go as high as a couple of hundred kHz frequency, which enables us to see how the adiabaticity breaks. Notice that when we say "adiabaticity" we refer only to the state of the system at $t = \frac{1}{2f}$ compared to the initial state, and discard the dynamics of the process.

are: $|0\rangle = |1,0\rangle$, $|+\rangle = e^{i\frac{\phi_\epsilon}{2}}|1,1\rangle + e^{-i\frac{\phi_\epsilon}{2}}|1,-1\rangle$ and $|-\rangle = e^{i\frac{\phi_\epsilon}{2}}|1,1\rangle - e^{-i\frac{\phi_\epsilon}{2}}|1,-1\rangle$ where ϕ_ϵ comes from the strain field [20]. We can utilize this fact to gain a deeper understanding of the strain field (using an ensemble) or even the local strain field (using a single NV setup).

To conclude, this new setup will enable us to explore fundamentals physics, increase coherence time, extend current knowledge regarding strain fields in the diamond lattice, measure external fields with high sensitivity, and generally make very exciting physics.

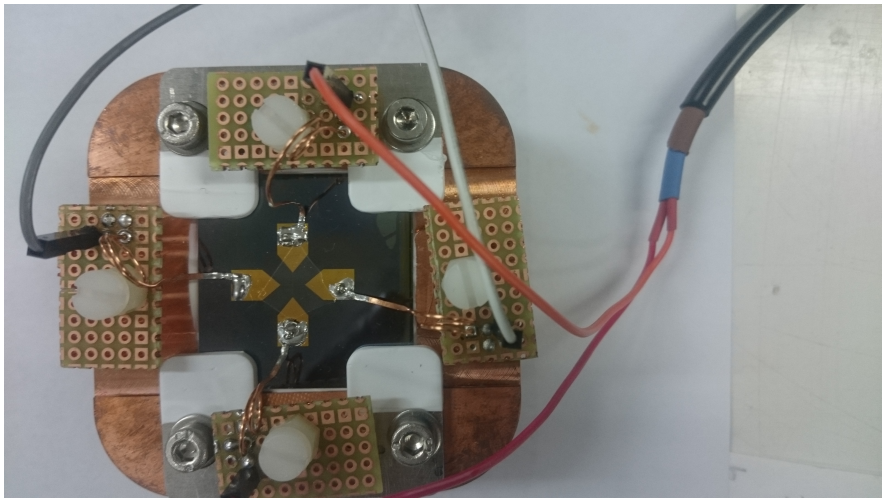

Figure C.2: Adiabaticity chip. The gold pads are connected to a current supply. The gold crossing wires that connect the pads are just 10 μm wide and therefore hardly noticeable in this figure. The transparent material above the pads is not the diamond but rather a simple cover glass to protect the thin gold wires. A [110] surface diamond would be placed above the wires for these anticipated experiments. By controlling the currents in the wires we can manipulate the effective magnetic field in the plane above the wires to generate rotation along the z axis or the $x-y$ plane with respect to a specific NV orientation. Image taken by the Ph.D student Yechezkel Schlussel.

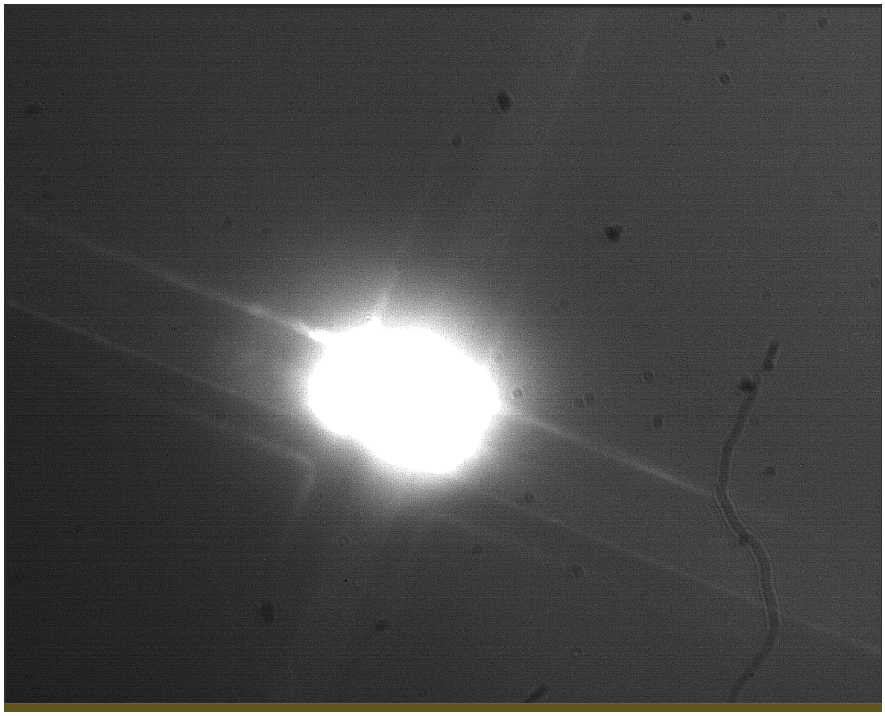

Figure C.3: The adiabaticity chip with a laser illuminating the wires junction. The sharp corners that can be seen just below the laser are SU-8 surfaces roughly 5 μm above the surface to support the diamond so that it will not scratch the thin gold wires. We chose a gap of 5 μm, where the magnetic field reaches its maximum amplitude. Since the laser beam is larger than the junction area we will install either a single-mode fiber before the objective for better focusing, or we will use a pinhole in order to collect red fluorescence from just the center of the junction. Image taken by the Ph.D student Yechezkel Schlussel.

Bibliography

[1] A Waxman. *Sensitive Magnetometry Based on NV Centers in Diamonds*. PhD thesis, Ben Gurion University, 2014.

[2] JR Maze, PL Stanwix, JS Hodges, S Hong, JM Taylor, P Cappellaro, L Jiang, MV Gurudev Dutt, E Togan, AS Zibrov, et al. Nanoscale magnetic sensing with an individual electronic spin in diamond. *Nature*, 455(7213):644–647, 2008.

[3] LM Pham, N Bar-Gill, D Le Sage, C Belthangady, A Stacey, M Markham, DJ Twitchen, MD Lukin, and RL Walsworth. Enhanced metrology using preferential orientation of nitrogen-vacancy centers in diamond. *Phys. Rev. B: Condens. Matter*, 86(12):121202, 2012.

[4] P Deák, B Aradi, M Kaviani, T Frauenheim, and A Gali. Formation of nv centers in diamond: A theoretical study based on calculated transitions and migration of nitrogen and vacancy related defects. *Phys. Rev. B*, 89(7):075203, 2014.

[5] T Nöbauer, K Buczak, A Angerer, S Putz, G Steinhauser, J Akbarzadeh, H Peterlik, J Majer, J Schmiedmayer, and M Trupke. Creation of ensembles of nitrogen-vacancy centers in diamond by neutron and electron irradiation. *arXiv preprint arXiv:1309.0453*, 2013.

[6] VM Acosta, E Bauch, MP Ledbetter, C Santori, K-MC Fu, PE Barclay, RG Beausoleil, H Linget, JF Roch, F Treussart, et al. Diamonds with a high density of nitrogen-vacancy centers for magnetometry applications. *Phys. Rev. B*, 80(11):115202, 2009.

[7] K Ohno, FJ Heremans, LC Bassett, BA Myers, DM Toyli, ACB Jayich, C J Palmstrøm, and D Awschalom. Engineering shallow spins in diamond with nitrogen delta-doping. *Appl. Phys. Lett.*, 101(8):082413, 2012.

[8] J Martin, R Wannemacher, J Teichert, L Bischoff, and B Köhler. Generation and detection of fluorescent color centers in diamond with submicron resolution. *Appl. Phys. Lett.*, 75(20):3096–3098, 1999.

[9] A Waxman, Y Schlussel, D Groswasser, VM Acosta, L-S Bouchard, D Budker, and R Folman. Diamond magnetometry of superconducting thin films. *Phys. Rev. B*, 89(5):054509, 2014.

[10] J Loubser and J van Wyk. Electron spin resonance in the study of diamond. *Rep. Prog. Phys.*, 41(8):1201, 1978.

[11] A Lenef and SC Rand. Electronic structure of the n-v center in diamond: Theory. *Phys. Rev. B: Condens. Matter*, 53(20):13441, 1996.

[12] Charles Kittel. *Introduction to solid state physics*. Wiley, 2005.

[13] Morton Hamermesh. *Group theory and its application to physical problems*. Courier Corporation, 1989.

[14] Lowell H Hall et al. Group theory and symmetry in chemistry. 1969.

[15] Peter W Atkins and Ronald S Friedman. *Molecular quantum mechanics*. Oxford university press, 2011.

[16] JR Maze, Adam Gali, Emre Togan, Yiwen Chu, Alexei Trifonov, Efthimios Kaxiras, and MD Lukin. Properties of nitrogen-vacancy centers in diamond: the group theoretic approach. *Phys. Rev. B*, 13(2):025025, 2011.

[17] A Gali, M Fyta, and E Kaxiras. Ab initio supercell calculations on nitrogen-vacancy center in diamond: Electronic structure and hyperfine tensors. *Phys. Rev. B*, 77(15):155206, 2008.

[18] LJ Rogers, RL McMurtrie, MJ Sellars, and NB Manson. Time-averaging within the excited state of the nitrogen-vacancy centre in diamond. *New J. Phys.*, 11(6):063007, 2009.

[19] G De Lange, ZH Wang, D Riste, VV Dobrovitski, and R Hanson. Universal dynamical decoupling of a single solid-state spin from a spin bath. *Science*, 330(6000):60–63, 2010.

[20] MW Doherty, F Dolde, H Fedder, F Jelezko, J Wrachtrup, NB Manson, and LCL Hollenberg. Theory of the ground-state spin of the nv- center in diamond. *Phys. Rev. B: Condens. Matter*, 85(20):205203, 2012.

[21] K Jensen, N Leefer, A Jarmola, Y Dumeige, VM Acosta, P Kehayias, B Patton, and D Budker. Cavity-enhanced room-temperature magnetometry using absorption by nitrogen-vacancy centers in diamond. *Phys. Rev. Lett.*, 112(16):160802, 2014.

[22] ML Goldman, A Sipahigil, MW Doherty, NY Yao, SD Bennett, M Markham, DJ Twitchen, NB Manson, A Kubanek, and MD Lukin. Phonon-induced population dynamics and intersystem crossing in nitrogen-vacancy centers. *Phys. Rev. B: Condens. Matters*, 114(14):145502, 2015.

[23] L Robledo, H Bernien, T van der Sar, and R Hanson. Spin dynamics in the optical cycle of single nitrogen-vacancy centres in diamond. *New J. Phys.*, 13(2):025013, 2011.

[24] JP Tetienne, L Rondin, P Spinicelli, M Chipaux, T Debuisschert, JF Roch, and V Jacques. Magnetic-field-dependent photodynamics of single nv defects in diamond: an application to qualitative all-optical magnetic imaging. *New J. Phys.*, 14(10):103033, 2012.

[25] K Jensen, VM Acosta, A Jarmola, and D Budker. Light narrowing of magnetic resonances in ensembles of nitrogen-vacancy centers in diamond. *Phys. Rev. B: Condens. Matter*, 87(1):014115, 2013.

[26] A Dréau, M Lesik, L Rondin, P Spinicelli, O Arcizet, J-F Roch, and V Jacques. Avoiding power broadening in optically detected magnetic resonance of single nv defects for enhanced dc magnetic field sensitivity. *Phys. Rev. B*, 84(19):195204, 2011.

[27] LM Pham. *Magnetic field sensing with nitrogen-vacancy color centers in diamond*. PhD thesis, Harvard University, 2013.

[28] RS Schoenfeld and W Harneit. Real time magnetic field sensing and imaging using a single spin in diamond. *Phys. Rev. Lett.*, 106(3):030802, 2011.

[29] L Rondin, JP Tetienne, T Hingant, JF Roch, P Maletinsky, and V Jacques. Magnetometry with nitrogen-vacancy defects in diamond. *Rep. Prog. Phys.*, 77(5):056503, 2014.

[30] P Kehayias, M Mrózek, VM Acosta, A Jarmola, DS Rudnicki, R Folman, W Gawlik, and D Budker. Microwave saturation spectroscopy of nitrogen-vacancy ensembles in diamond. *Phys. Rev. B: Condens. Matter*, 89(24):245202, 2014.

[31] A Laraoui, F Dolde, C Burk, F Reinhard, J Wrachtrup, and CA Meriles. High-resolution correlation spectroscopy of 13c spins near a nitrogen-vacancy centre in diamond. *Nat. Commun.*, 4:1651, 2013.

[32] N Bar-Gill, LM Pham, C Belthangady, D Le Sage, P Cappellaro, JR Maze, MD Lukin, A Yacoby, and R Walsworth. Suppression of spin-bath dynamics for improved coherence of multi-spin-qubit systems. *Nat. Commun.*, 3:858, 2012.

[33] VM Acosta, E Bauch, MP Ledbetter, A Waxman, L-S Bouchard, and D Budker. Temperature dependence of the nitrogen-vacancy magnetic resonance in diamond. *Phys. Rev. Lett.*, 104(7):070801, 2010.

[34] A Yariv. Quantum electronics, 3rd. *Edn.(Wiely, New York, 1988)*, Chapter 14.

[35] J Zhou, P Huang, Q Zhang, Z Wang, T Tan, X Xu, F Shi, X Rong, S Ashhab, and J Du. Observation of time-domain rabi oscillations in the landau-zener regime with a single electronic spin. *Phys. Rev. Lett.*, 112(1):010503, 2014.